

PA 55,692

TACTEC

PA 55,692 TP

MEMORANDUM REPORT BRL-MR-3676

BRL

1938 - Serving the Army for Fifty Years - 1988

PREDICTED LOADING FROM A 241.kPa (35 PSI)
BLAST WAVE ON A CANDIDATE RAREFACTION
WAVE ELIMINATOR

RICHARD E. LOTTERO
JOHN D. WORTMAN

JUNE 1988

APPROVED FOR PUBLIC RELEASE; DISTRIBUTION UNLIMITED.

U.S. ARMY LABORATORY COMMAND

BALLISTIC RESEARCH LABORATORY
ABERDEEN PROVING GROUND, MARYLAND

REC'D JUL 06 1988

DESTRUCTION NOTICE

Destroy this report when it is no longer needed. DO NOT return it to the originator.

Additional copies of this report may be obtained from the National Technical Information Service, U.S. Department of Commerce, Springfield, VA 22161.

The findings of this report are not to be construed as an official Department of the Army position, unless so designated by other authorized documents.

The use of trade names or manufacturers' names in this report does not constitute indorsement of any commercial product.

REPORT DOCUMENTATION PAGE				Form Approved OMB No. 0704-0188		
1a. REPORT SECURITY CLASSIFICATION (Unclassified)			1b. RESTRICTIVE MARKINGS			
2a. SECURITY CLASSIFICATION AUTHORITY			3. DISTRIBUTION / AVAILABILITY OF REPORT			
2b. DECLASSIFICATION / DOWNGRADING SCHEDULE						
4. PERFORMING ORGANIZATION REPORT NUMBER(S) (BRL-MR-3676)			5. MONITORING ORGANIZATION REPORT NUMBER(S)			
6a. NAME OF PERFORMING ORGANIZATION Army Ballistic Research Laboratory		6b. OFFICE SYMBOL (If applicable) SLCBR-TB	7a. NAME OF MONITORING ORGANIZATION			
6c. ADDRESS (City, State, and ZIP Code) Aberdeen Proving Ground, MD 21005-5066			7b. ADDRESS (City, State, and ZIP Code)			
8a. NAME OF FUNDING / SPONSORING ORGANIZATION (Harry Diamond Laboratories)		8b. OFFICE SYMBOL (If applicable) SLCHD-NW-P	9. PROCUREMENT INSTRUMENT IDENTIFICATION NUMBER			
8c. ADDRESS (City, State, and ZIP Code) 2800 Powder Mill Road Adelphi, Maryland 20783-1197 MD			10. SOURCE OF FUNDING NUMBERS			
			PROGRAM ELEMENT NO. 612120.AH25	PROJECT NO. 44061- 801-63	TASK NO.	WORK UNIT ACCESSION NO.
11. TITLE (Include Security Classification) (PREDICTED LOADING FROM A 241.3 KPA (35 PSI), 600 KT BLAST WAVE ON A CANDIDATE RAREFACTION WAVE ELIMINATOR)						
12. PERSONAL AUTHOR(S) (Lottero, Richard E. and Wortman, John D.)						
13a. TYPE OF REPORT (Final Report)		13b. TIME COVERED FROM 87/10/01 to 88/04/30		14. DATE OF REPORT (Year, Month, Day) (June 1988)		15. PAGE COUNT (44)
16. SUPPLEMENTARY NOTATION						
17. COSATI CODES			18. SUBJECT TERMS (Continue on reverse if necessary and identify by block number)			
FIELD 15	GROUP 06	SUB-GROUP	Airblast; Rarefaction Wave Eliminator; Full Hydrocode; Blast; Simulator; Blast Loading; RWE			
19. ABSTRACT (Continue on reverse if necessary and identify by block number) (This study provides estimates of the blast loading on a candidate passive Rarefaction Wave Eliminator (RWE) design for the proposed US Large Blast/Thermal Simulator (LB/TS). This design includes an Interior RWE (I-RWE) that has a fixed blockage of the flow area, and a Primary RWE (P-RWE) with adjustable blockage settings. Also included in this design are two sets of side vents which can be either completely closed or opened, depending on the design test conditions. The set of side vents located between the I-RWE and the P-RWE is termed the Downstream Side Vent (DSV), and the set of side vents located upstream from the I-RWE is termed the Upstream Side Vent (USV). Hydrocode computations were performed assuming a 241.3 kPa (35 psi) peak overpressure blast wave from a 600 KT device for both the normal operation settings of minimum RWE blockage and maximum side vent openings, and for an assumed accident situation where the P-RWE presented a maximum possible blockage and the side vents were closed. The net horizontal forces on both the I-RWE and P-RWE are computed as functions (Continued)						
20. DISTRIBUTION / AVAILABILITY OF ABSTRACT <input type="checkbox"/> UNCLASSIFIED/UNLIMITED <input checked="" type="checkbox"/> SAME AS RPT. <input type="checkbox"/> DTIC USERS			21. ABSTRACT SECURITY CLASSIFICATION Unclassified			
22a. NAME OF RESPONSIBLE INDIVIDUAL Richard E. Lottero and John D. Wortman			22b. TELEPHONE (Include Area Code) (301) 278-6035/6028		22c. OFFICE SYMBOL SLCBR-TB-B	

19. ABSTRACT (Continued)

of time for both cases, as are the mass flow rates through the test section, the I-RWE, P-RWE, USV, and DSV. An analysis of the resulting wave interactions in the LB/TS near the RWE end is also presented, including a discussion of the pressure loading on the individual sections of the side walls of the LB/TS in that region. >

Acknowledgement

The small-scale experimental studies of various passive RWE's were conceived and performed by C. Kingery and G. Coulter. The scale-up to the size of the LB/TS of these designs was performed by R. Pearson. W. D. Allison kindly lent much support in the use of the TROFF utility initially used to produce this document. P. Broome, J. Walter, R. Cahoon, and J. Kuzan lent much support in the use of the L^AT_EX Document Publishing System [23] finally used to produce this document. The support of these BRL colleagues as well as the support of others is gratefully acknowledged.

Table of Contents

	<u>Page</u>
List of Figures	vii
I. Introduction	1
II. The Hydrocode Computations	2
III. Loading on the Rarefaction Wave Eliminators	4
1. Primary RWE	4
a. Overpressure on the Primary RWE	4
b. Force on the Primary RWE	5
2. Interior RWE	5
a. Overpressure on the Interior RWE	5
b. Force on the Interior RWE	6
IV. Mass Flux in the LB/TS	6
1. Net Mass Flux in the LB/TS as a System	6
2. Mass Flux through the Interior RWE	7
3. Individual Mass Fluxes for the Normal Vent Computation	8
V. Overpressure on LB/TS Side Wall Sections	8
1. Side Wall between the Downstream Side Vent and the Primary RWE	8
2. Side Wall between the Interior RWE and the Downstream Side Vent	8
3. Side Wall between the Upstream Side Vent and the Interior RWE	9
4. Side Wall from the Start of the Thick Wall Section to the Upstream Side Vent	9
5. Entire Thick Side Wall Section, Excluding Open or Closed Side Vents	10
VI. Test Station	10
VII. Conclusion	10
List of References	43
Distribution List	45

List of Figures

<u>Figure</u>	<u>Page</u>
1a A Simplified Schematic of the Proposed US LB/TS. (Courtesy of R. Pearson.)	12
1b Proposed LB/TS Cross-Section. (Courtesy of R. Pearson.)	13
2 Axial Section through the Expansion Tunnel (Section A-A in Figure 3). (Courtesy of R. Pearson.)	14
3 Exit Plane of the Primary Rarefaction Wave Eliminator (Section D-D in Figure 2). (Courtesy of R. Pearson.)	15
4 Two Candidate Shapes of the Vanes for the Primary Rarefaction Wave Eliminator.	16
5 Tunnel Cross Section Looking Upstream at the Interior Rarefaction Wave Eliminator (Section C-C in Figure 2). (Courtesy of R. Pearson.)	17
6a Average Overpressure on the P-RWE, Low Vent.	18
6b Average Overpressure on the P-RWE, Normal Vent.	19
7a Axial Forces on the P-RWE, Low Vent.	20
7b Axial Forces on the P-RWE, Normal Vent.	21
8a Average Overpressure on the I-RWE, Low Vent.	22
8b Average Overpressure on the I-RWE, Normal Vent.	23
9a Axial Forces on the I-RWE, Low Vent.	24
9b Axial Forces on the I-RWE, Normal Vent.	25
10a Mass Flux in the LB/TS as a Control Volume, Low Vent.	26
10b Mass Flux in the LB/TS as a Control Volume, Normal Vent.	27
11a Mass Flux through the I-RWE, Low Vent.	28
11b Mass Flux through the I-RWE, Normal Vent.	29
12 Mass Fluxes for Each Flow Area, Normal Vent.	30
13a Average Overpressure on the LB/TS Side Wall between the DSV and the P-RWE, Low Vent.	31
13b Average Overpressure on the LB/TS Side Wall between the DSV and the P-RWE, Normal Vent.	32

List of Figures (Continued)

<u>Figure</u>	<u>Page</u>
14a Average Overpressure on the LB/TS Side Wall between the I-RWE and the DSV, Low Vent.	33
14b Average Overpressure on the LB/TS Side Wall between the I-RWE and the DSV, Normal Vent.	34
15a Average Overpressure on the LB/TS Side Wall between the USV and the I-RWE, Low Vent.	35
15b Average Overpressure on the LB/TS Side Wall between the USV and the I-RWE, Normal Vent.	36
16a Average Overpressure on the LB/TS Side Wall from the Start of the Thick Wall Section to the USV, Low Vent.	37
16b Average Overpressure on the LB/TS Side Wall from the Start of the Thick Wall Section to the USV, Normal Vent.	38
17a Average Overpressure on the LB/TS Thick Side Wall Section, Excluding Closed Side Vent Areas, Low Vent.	39
17b Average Overpressure on the LB/TS Thick Side Wall Section, Excluding Open Side Vent Areas, Normal Vent.	40
18a Average Overpressure across the LB/TS Cross-Sectional Area at the Test Station, Low Vent.	41
18b Average Overpressure across the LB/TS Cross-Sectional Area at the Test Station, Normal Vent.	42

I. Introduction

Since the construction of the Large Blast Simulator (LBS) in Gramat, France [1], the United States has been actively engaged in developing a design for a Large Blast/Thermal Simulator (LB/TS) [2-10]. The primary purpose of this part of the design study was to estimate the blast loading on a candidate passive Rarefaction Wave Eliminator (RWE) design for the proposed US LB/TS. This passive RWE design concept and others were conceived and tested at small scale at the BRL [11], and scaled up to the LB/TS [12]. The RWE is located at the discharge end of the LB/TS. Its purpose is to prevent, or at least minimize, the generation of upstream-traveling rarefaction waves caused by the interaction of the blast wave with the ambient air outside of the LB/TS by a combination of partially reflecting the incident shock and by acting as a valve to control the flow. Otherwise, these waves could travel upstream against a subsonic flow and distort the remainder of the blast wave at the test station. A simplified schematic of the proposed US LB/TS is shown (not to scale) in Figure 1a, and a cross-section of the LB/TS is shown in Figure 1b. This design includes an Interior (upstream) RWE (hereinafter referred to as the I-RWE) that has a set amount of blockage caused by fixed vertical bars equal to 20 percent of the cross-sectional area of the LB/TS test section, and a Primary RWE (hereinafter referred to as the P-RWE) with adjustable blockage settings from 31.5 percent to 80 percent of the LB/TS cross-sectional area at the exit of the expansion tunnel (see Figure 2). A drawing of the P-RWE is shown in Figure 3, with cross-sections of two generic candidate shapes for a single vane shown in Figure 4. A drawing of the I-RWE is shown in Figure 5. Also included in this design are two sets of side vents which can be either completely closed, or opened to a combined maximum of 61.5 percent of the LB/TS cross-sectional area (see Figure 2). The set of side vents located between the I-RWE and the P-RWE is termed the Downstream Side Vent (hereinafter referred to as the DSV), and the set of side vents located upstream from the I-RWE is termed the Upstream Side Vent (USV). The DSV is necessary to provide additional venting area to compensate for the unavoidable blockage (a minimum of 31.5 percent) of the P-RWE in its fully opened position. The USV provides similar additional venting to compensate for the fixed 20 percent blockage of the I-RWE.

A second purpose of this study was to estimate the overpressure buildup at the end of the LB/TS near the RWE's, particularly in a situation where the combined open areas of the P-RWE, USV, and DSV are too small for the planned blast wave. The strongest blast wave currently planned for simulation in the LB/TS is a 241.3 kPa (35 psi) peak overpressure blast wave from a 600 KT nuclear burst above ground, so this wave was chosen for this study. Two hydrocode computations were run, one assuming "correct" P-RWE and side vent flow area settings equal to a total of 130 percent of the LB/TS cross-sectional area, and another assuming an accidental "worst case" P-RWE and side vent total flow area setting equal to 20 percent of the LB/TS cross-sectional area. The computation using the correct P-RWE settings was assigned problem number 8606.02. For simplicity, this computation will hereinafter be referred to as the "normal vent" computation. The computation using the presumed worst case vent area was assigned problem number 8605.27. For simplicity, this computation will hereinafter be referred to as the "low vent" computation. These computations are described in the next section.

II. The Hydrocode Computations

The BRL version [13-14] of the HULL [15] hydrodynamic computer code was used for the numerical propagation of the blast wave down the LB/TS and its interaction with the RWE's and side vent areas. This version of the HULL hydrocode solves the inviscid Euler equations by using a modified Lax-Wendroff, explicit time step, finite difference method. HULL is actually a large collection of cooperative programs and shared subroutines. Its principal programs are a grid generator KEEL, the hydrocode HULL, and a plotting utility PULL. This version of HULL can be set up to run using either three-dimensional (3-D) or two-dimensional (2-D) Cartesian coordinates, or 2-D cylindrical coordinates having rotational symmetry. All flow field cells in 3-D Cartesian coordinates must be either entirely filled with hydrodynamic material or designated as non-hydrodynamic and rigid ("island") cells. Flow field cells in the 2-D versions may also be of either type, and may additionally be half hydrodynamic and half island ("shore") [14]. All cells in all versions must have a rectangular cross-section.

In order to make the hydrocode computations more tractable, a geometric simplification was made. Although the problem in the actual LB/TS is inherently 3-D (see Figure 1), most of the principal features of the flow for this problem of determining RWE blast loading can be approximated well in 2-D HULL with cylindrical coordinates. The problem was transformed into an axially symmetric problem, with a cylindrical shock tube having a radius equal to the hydraulic radius of the LB/TS. The hydraulic radius is equal to the cross-sectional area of the LB/TS divided by its perimeter. Flow and blockage areas for the I-RWE and P-RWE were transformed into spaced concentric toroidal rings of either hydrodynamic or island cells, and the two bands of discrete side vents which comprise the USV and DSV were transformed into radial vent bands around the entire circumference of the transformed LB/TS. The side wall of the LB/TS, except for the open bands representing the side vents, was simulated by a rigid, impermeable shell made up of island cells. The drivers were not simulated, but rather the LAMB [16] code, a set of empirical fits based in part on the 1 KT Standard [17], was used as the upstream input boundary condition to feed the 241.3 kPa, 600 KT, decaying blast wave into the HULL hydrocode grid as time progressed. A similar feed-in of a LAMB blast wave through the same type of transmissive boundary is discussed in a previous study [18] on shock tube blockage effects. The loading on the RWE's is produced not only by the direct effect of the interaction of the blast wave, but is also enhanced by the blockage effects documented in previous work [18-22].

The low vent hydrocode computation was for the worst case situation where both the USV and DSV were closed and the P-RWE was only open to 20 percent of the LB/TS cross-sectional area (i.e., 80 percent closed). The normal vent hydrocode computation was for the situation where the P-RWE and the side vents were set at their design positions for this blast wave: 68.5 percent open for the P-RWE, 16.6 percent of the test section area for the DSV, and 44.9 percent of the test section area for the USV. These openings all represent maximum possible openings under this design concept. The I-RWE flow area was fixed at 80 percent of the LB/TS cross-sectional area (i.e., 20 percent closed) for both computations. Both computations used the same basic grid design, including having identical flow field computational cell sizes, with the only variations being those necessary to simulate the differences in side vent areas and P-RWE settings. These differences were a matter of

defining some cells in the LB/TS side wall as either hydrodynamic cells for the normal vent case through which material could flow, or island cells for the low vent case which created a barrier to the flow. A large free field was defined outside of the LB/TS so that outflow from the LB/TS would not be artificially interfered with by the computational boundaries of the grid.

It should be noted that the exact dimensions and locations used in these computations are not necessarily design values for the LB/TS, but in some cases are the results of the geometric simplifications introduced into the problem to make a more tractable computation using a cylindrically symmetric geometry in the HULL hydrocode. The essentials of the grids in the axial direction, a total of 458 cells, are listed below:

1. A 210 cell region defined as Set A, from the start of the grid (axially) at 0.0 m to 51.7120 m, which includes the test station at 20.0000 m. (Note that this zero point is not the true start of the LB/TS expansion section, but is used simply as a matter of convenience for these computations. The quotation of four significant figures beyond the decimal point is done to give an indication of the sizing of the flow field cells.) The normal wall thickness in the LB/TS ends at 51.7120 m, which is the beginning of the thick wall section at the RWE end of the expansion section. The current design for the LB/TS calls for the last several meters of the expansion section to be approximately 1.22 m (4.0 feet) thick. This section serves in an additional capacity as a carrier of anchoring cables for the P-RWE. The thickness of the LB/TS wall is not directly relevant to these computations. It is modeled as 0.862 m thick throughout its entire length.
2. A 69 cell region, Set B, from 51.7120 m to 62.4659 m, which includes the thick wall section upstream from the USV. The HULL hydrocode computation is started with the shock front located in this Set at 61.9575 m for both computations.
3. A 16 cell region, Set C, from 62.4659 m to 64.0929 m, whose intersect with Set L (see the radial grid description below) simulates the open span in the LB/TS side wall for the USV in the normal vent problem. The open area is equal to 44.9 percent of the LB/TS cross-sectional area. The intersect of this Set with Set L is a solid wall for the low vent problem.
4. A nine cell region, Set D, from 64.0929 m to 65.0000 m, which simulates a solid side wall region between the USV and the I-RWE.
5. A six cell region, Set E, from 65.0000 m to 65.6600 m, which simulates the I-RWE, which blocks 20 percent of the LB/TS cross-sectional area for both computations. This blockage is simulated by a grouping of five concentric toroidal rings of island cells within the intersect of this Set and Set K.
6. A 20 cell region, Set F, from 65.6600 m to 67.6993 m, which simulates the region between the I-RWE and the DSV.
7. A six cell region, Set G, from 67.6993 m to 68.3008 m, whose intersect with Set L simulates the open area in the LB/TS side wall for the DSV in the normal vent problem. The open area is equal to 16.6 percent of the LB/TS cross-sectional area. The intersect of this Set with Set L is a solid wall for the low vent problem.

8. A 17 cell region, Set H, from 68.3008 m to 70.0000 m, which simulates the region between the DSV and the P-RWE at the end of the LB/TS.
9. An eight cell region, Set I, from 70.0000 m to 70.8440 m, which simulates the P-RWE. This is set to an opening equal to 20 percent of the LB/TS cross-sectional area for the low vent problem (i.e., 80 percent closed). It is set to an opening equal to 68.5 percent of the LB/TS cross-sectional area for the normal vent problem (i.e., 31.5 percent closed.) These different blockages are simulated by different choices of groupings of toroidal rings of island cells within the intersect of this Set and Set K.
10. A 97 cell region, Set J, from 70.8440 m to 102.389 m, which simulates the distance axially from the end of the P-RWE to the far downstream boundary in the axial direction.

The essentials of the grids in the radial direction, a total of 144 cells, are listed below:

1. A 60 cell region, Set K, from 0.0 m to 7.24715 m, which simulates the interior of the LB/TS from the origin to the LB/TS side wall. (Note that 7.24715 m is the hydraulic radius of the actual LB/TS.)
2. A six cell region, Set L, from 7.24715 m to 8.10925 m, which simulates the LB/TS side wall, typically with island cells except where side vents are simulated. This thickness was chosen to approximate the cross-sectional area of the side wall if it were uniformly distributed in a complete circular shell. This was an arbitrary decision. To keep the grid simple, the side wall was simulated to be of the same thickness throughout its length; any effect on the loadings of interest here because of this simplification would be negligible.
3. A 78 cell region, Set M, from 8.10925 m to 40.1679 m, which simulates the region between the outer surface of the LB/TS side wall and the outer radial boundary of the computational flow field.

III. Loading on the Rarefaction Wave Eliminators

1. Primary RWE

a. Overpressure on the Primary RWE

The overpressure on the P-RWE for the low vent problem is shown in Figure 6a. The values for average overpressure on the front and back faces are computed using only those flow field cells immediately adjacent to the island cells simulating the P-RWE itself. These values are then used to obtain the net axial average pressure acting on the P-RWE, subtracting the overpressure on the back from that on the front. The net overpressure curve shows a rapid rise to a peak average overpressure of 658.9 kPa (95.6 psi) at 85.4 ms, not too far from the peak theoretical overpressure of 850.2 kPa (123.3 psi) for normal reflection from a continuous wall. (Values quoted here and in subsequent discussions are from tabulated results.) There is then a subsequent rise to 704.4 kPa (102.2 psi) at 108.4 ms because of the

return of a partial reflection from the back face of the I-RWE, and a slow reduction in net pressure from that point. The time used for this plot, and all subsequent plots, is referenced to $t = 0.0$ at the incident shock arrival at the test station, located in both computations at the 20.0 m axial position as defined for purposes of these computations.

The overpressure on the P-RWE for the normal vent problem is shown in Figure 6b. The time of arrival of the shock is essentially the same as for the low vent problem, but the peak net overpressure on the P-RWE is 476.8 kPa (69.2 psi), 28 percent below the first peak for low venting. This lower peak is also relieved very rapidly, with no second peak from the back of the I-RWE because of the combined venting action of the DSV and the more open P-RWE. By the final point in time shown on this plot, 186.4 ms, the net overpressure is at 253.1 kPa (36.7 psi), still decreasing, and relatively close to the undisturbed peak incident shock overpressure of 241.3 kPa.

b. Force on the Primary RWE

Figure 7a shows the axial forces on the P-RWE for the low vent problem, including the front face force, back face force, and net force. Except for the scaling factor resulting from the multiplication by the area, the curves are similar to those for the average overpressure. The first peak net force on the P-RWE is 86.8 MN (19,500,000 lbf) at 85.4 ms, and the second peak force is 92.8 MN (20,900,000 lbf) at 108.4 ms. This may be impractical to design to, especially if a safety factor of at least 2.0 is applied.

Figure 7b shows a corresponding set of curves for axial forces on the P-RWE for the normal vent problem. Here, the peak forces are not only substantially less than for the low vent problem, but the relief action is also more rapid, as pointed out above. The peak net force on the P-RWE for the normal vent problem is 24.7 MN (5,550,000 lbf), occurring at 85.4 ms. This peak net force is 26.6 percent of that for the low vent case, due to the combined effects of having a lower peak overpressure and a smaller presented area, and should be a reasonably solvable design problem.

2. Interior RWE

a. Overpressure on the Interior RWE

The average overpressure on the I-RWE for the low vent problem is shown in Figure 8a, illustrating the front face and back face averages, and the net value obtained by subtracting the back face from the front face. The net overpressure curve shows several interesting features. There is a peak value of 658.8 kPa (95.6 psi) at 75.9 ms, which results from the partial reflection of the incident shock from the front face of the I-RWE, a rapid decrease to 344.7 kPa (50.0 psi) at 78.4 ms, a slow decrease to 295.8 kPa (42.9 psi) at 94.4 ms, a rapid decrease to a net negative value [in a directional sense] of [-]225.1 kPa ([-]32.6 psi) at 98.4 ms, and a small positive value of 7.4 kPa (1.1 psi) by 186.4 ms. The individual curves for the front and back face show that this behavior is caused by a strong pressure wave moving upstream. (Note the sudden rise in back face average overpressure starting at 94.4 ms.)

The average overpressure on the I-RWE for the normal vent problem is shown in Figure 8b. It is immediately apparent that the curves for the normal vent problem are distinctly different from those for the low vent problem. The initial peak overpressure for normal venting is 585.9 kPa (85.0 psi), which also occurs at 75.9 ms, but is less than that for low venting because for normal venting the incident shock must pass by the open USV prior to reaching the front face of the I-RWE. The incident shock is thereby weakened by expansion waves moving radially inward from the USV; the overpressure from the partial reflection of the incident shock on the I-RWE front face is also relieved more quickly for the same reason. A near-plateau around 300 kPa (43.5 psi) is reached in the net overpressure for the normal vent problem, lasting until about 98.4 ms. This is followed by a rather rapid decrease to 129.0 kPa (18.7 psi), then a slight increase and subsequent slow decrease to 118.3 kPa (17.2 psi) by the last point in time of 186.4 ms. This is caused by a sequence of reflected compression waves and expansion waves from the P-RWE, and expansion waves from the USV and DSV.

b. Force on the Interior RWE

The various curves for axial forces on the I-RWE for the low vent problem are shown in Figure 9a, including front face force, back face force, and net force. As noted previously in the discussion for the P-RWE, these curves are simply the average overpressure curves (see Figure 8a) scaled by area. The most interesting things that this set of curves highlights are the reversals of force on the I-RWE as time progresses. The peak net positive force (acting toward the P-RWE) is 21.9 MN (4,920,000 lbf) at 75.9 ms, followed by a later force reversal to a negative (acting toward the drivers) net force of 7.48 MN (1,680,000 lbf) at 98.4 ms caused by the strong wave reflection from the P-RWE. While these forces do not in themselves pose a particularly difficult design problem, care would be needed to design for a force reversal.

Figure 9b shows a corresponding set of curves for axial forces on the I-RWE for the normal vent problem. There is no force reversal here because there is no strong reflected wave from the P-RWE. The peak reflected net force on the I-RWE is 19.5 MN (4,380,000 lbf) at 75.9 ms, caused by the initial interaction with the incident shock wave. This peak then decays in the manner described for the overpressure curve for this case. These forces do not appear to pose any particularly difficult design problems, except for the need to properly design the anchors for the I-RWE in the expansion tunnel wall to handle both the forces and the moments that they generate.

IV. Mass Flux in the LB/TS

1. Net Mass Flux in the LB/TS as a System

A discussion of the mass flow in the LB/TS is warranted here because it helps to illustrate the extent to which the flows in the normal vent and low vent computations are different from one another. For the immediate purpose of this discussion, it is useful to consider the LB/TS, axially from the test station (at 20.0 m) to the end of the P-RWE, and

radially from the axis of symmetry to the side wall, as a control volume. Figure 10a shows a set of mass flux curves for the low vent problem. In the discussion that follows, positive mass flux is flow into the control volume and negative mass flux is flow out of the control volume. The mass flux into the control volume in this case is the mass flow across the test station, which is always positive and decreases monotonically with time. The negative phase that would occur in a real blast wave is ignored in this study. The low vent problem has no side venting, so the mass flow out is only through the restricted 20 percent opening in the P-RWE. The start of mass flow through the P-RWE can be seen in the curve labeled "OUT" in Figure 10a by a change to negative mass flow from no flow at 83.4 ms. The net mass flow curve shows immediately why the overpressure and force curves behaved as they did. During all of the time simulated so far, there is a large mass accumulation due to the positive net mass flow into this control volume, specifically in the RWE end of the LB/TS. The peak mass flow rate into the control volume occurs upon the passage of the incident shock by the test station. The peak mass flow rate shown here in Figure 10a, 124.6 Mg/s (275,000 lbm/s), is less than the mass flow rate immediately behind the shock as it passes the test station because both computations were started with the shock well past the test station, just upstream from the closed USV. A high-pressure, high-density region is still expanding in the upstream direction at 186.4 ms, the current ending time of the computation, with the mass still accumulating at the rate of 82.5 Mg/s (182,000 lbm/s).

Figure 10b shows a similar set of curves for mass flux for the normal vent case, showing mass flux in, mass flux out, and net mass flux. A comparison of these curves with those in Figure 10a shows why the flows in the two problems are so different from one another. The normal vent problem has only a relatively brief mass accumulation period because the blast wave almost immediately passes by the open USV, and then quickly reaches the open DSV, and finally the more open P-RWE. (The individual mass flows through the test station, side vents, and P-RWE are discussed in Subsection IV.3 below.) The net mass flux becomes negative at 85.4 ms, very soon after the incident shock arrives at the P-RWE. It stays negative for the remainder of the computation time.

2. Mass Flux through the Interior RWE

Figure 11a shows the mass flux through the I-RWE for the low vent problem, and gives another good illustration of the action of the strong reflected wave which is moving upstream. The peak mass flow through the I-RWE is 121.8 Mg/s (269,000 lbm/s), occurring at 75.9 ms, which is coincident with the arrival of the incident shock at the I-RWE. This is not equal to the peak mass flux of the blast wave itself because of the 20 percent blockage of the I-RWE. The slow decrease of the mass flux with time is relatively constant until 98.4 ms, and is due primarily to a combination of the decay rate of the blast wave and the partial reflection of the incident shock from the I-RWE. After this time, the strong reflected wave (see Figure 8a) from the P-RWE arrives at the back face of the I-RWE, decreasing the mass flow rate from 115.0 Mg/s (254,000 lbm/s) at 98.4 ms to 44.0 Mg/s (97,000 lbm/s) at 104.4 ms, and to 23.6 Mg/s (52,000 lbm/s) by the ending time of 186.4 ms.

The curve for mass flow through the I-RWE for the normal vent problem, shown in Figure 11b, is markedly different from that for the low vent problem. It has a peak value

of 113.2 Mg/s (250,000 lbm/s) at 76.4 ms, somewhat below that for the low vent problem because of the action of the USV. The curve then shows a relatively smooth monotonic decline with time, with only a slight perturbation around 110 ms.

3. Individual Mass Fluxes for the Normal Vent Computation

Figure 12 shows the mass fluxes for each individual flow area for the normal vent problem. The curve labeled "USV" represents the mass flux through the USV; its greatest mass flux out is 35.3 Mg/s (77,800 lbm/s). The curve labeled "DSV" represents the mass flux through the DSV; its greatest mass flux out is 14.6 Mg/s (32,200 lbm/s). The peak mass flux out for the P-RWE is 89.3 Mg/s (197,000 lbm/s) at 86.4 ms corresponding to the incident shock arrival at the P-RWE. The mass flux at the test station is also shown for reference.

V. Overpressure on LB/TS Side Wall Sections

1. Side Wall between the Downstream Side Vent and the Primary RWE

Figure 13a shows the average overpressure on the LB/TS side wall between the closed DSV and the P-RWE for the low vent problem. The solid curve shows the net pressure on the wall. The first peak of 658.3 kPa (95.5 psi) at 91.4 ms is followed by a second peak of 677.3 kPa (98.2 psi) at 108.4 ms, and then a gradual decrease from that point. The average pressure is still quite high at 513.3 kPa (74.4 psi) at the ending time of 186.4 ms, still over two times the incident shock overpressure. This is due to the combined effects of the pressure rise from the reflection of the incident shock wave from the P-RWE and the limited venting.

Figure 13b shows the average overpressure for the same wall section for the normal vent problem. Here, there is a single peak overpressure of 347.6 kPa (50.4 psi) at 92.4 ms, 48.7 percent less than the highest peak for the low vent problem. The decay from the peak for the normal vent problem is more rapid than that for the low vent problem. The last value for overpressure at 186.4 ms is 198.0 kPa (28.7 psi).

2. Side Wall between the Interior RWE and the Downstream Side Vent

Figure 14a shows the average overpressure on the LB/TS side wall between the I-RWE and the upstream end of the closed DSV for the low vent problem. The first peak in the net pressure curve, 214.6 kPa (31.3 psi) at 80.4 ms, is due to the passage of the incident shock front after it passed through the I-RWE. After a brief decline in pressure, there is a rapid rise due to the movement upstream of the reflected wave from the P-RWE, reaching a peak of 649.1 kPa (94.1 psi) at 116.4 ms, and then decreasing from that point.

Figure 14b shows a similar set of overpressure curves for the normal vent problem. A comparison between Figures 14a and 14b shows the great difference in the net side wall pressure for the normal vent problem as opposed to the low vent problem. The first peak

net pressure is 177.4 kPa (25.7 psi) at 80.4 ms, followed by a subsequent peak of 241.2 kPa (35.0 psi) at 106.4 ms, and then a gradual decrease to 171.4 kPa (24.9 psi) by 186.4 ms.

3. Side Wall between the Upstream Side Vent and the Interior RWE

Figure 15a shows a set of curves for average overpressure on the LB/TS side wall between the closed USV and the I-RWE for the low vent problem. After an initial peak of 376.7 kPa (54.6 psi) at 82.4 ms due to the passage of the incident shock and its subsequent partial reflection from the front face of the I-RWE, the net pressure reaches a maximum of 660.0 kPa (95.7 psi) at 119.4 ms. This sustained second high pressure is caused by the tube filling process discussed earlier. The net pressure is 512.3 kPa (74.3 psi) at the 186.4 ms ending time.

Figure 15b shows a corresponding set of overpressure curves for the normal vent problem. The initial peak net pressure is 368.4 kPa (53.4 psi) at 83.4 ms, relatively close to the initial peak for the low vent problem. There is an initial decrease, a second peak of 354.2 kPa (51.4 psi) at 114.4 ms, and then a decrease to 265.3 kPa (38.5 psi) by 186.4 ms, which is considerably lower than the comparable net pressure for the low vent problem. The initial decreases are due primarily to the relieving action of the USV, and the subsequent decreases are due to the combined effects of the larger vent areas relative to the low vent case.

4. Side Wall from the Start of the Thick Wall Section to the Upstream Side Vent

Figure 16a shows a set of curves for the overpressure on the LB/TS side wall from the start of the thick wall section to the start of the closed USV for the low vent problem. The initial decline in the net pressure from 225.1 kPa (32.6 psi) at 70.6 ms to 223.4 kPa (32.4 psi) at 89.4 ms is due to the normal decay of the blast wave. There is a subsequent set of two rises, leading to a peak of 590.9 kPa (85.7 psi) at 146.4 ms. The first rise is from the reflection of the incident shock from the I-RWE, and the second rise is from its reflection from the P-RWE. There is then a decline to 515.2 kPa (74.7 psi) by 186.4 ms due to the venting through the P-RWE.

Figure 16b shows a corresponding set of curves for the normal vent problem. The net pressure curve shows only minor disturbances starting at approximately 110 ms; it is otherwise similar to what the pressures would be in a very long LB/TS with no internal area changes or reflecting surfaces. The initial peak average net pressure is 233.6 kPa (33.9 psi) at 71.7 ms, followed by a monotonic decrease to 188.3 kPa (27.3 psi) by 186.4 ms. Thus, it appears that the combined settings of open areas for the I-RWE, P-RWE, USV, and DSV allow the passage of the blast wave through the LB/TS with a minimum of disturbance. This represents one possible approach, but not necessarily the only means of allowing the blast wave to exit the expansion section without generating perturbations in the wave that could propagate upstream to the test station.

5. Entire Thick Side Wall Section, Excluding Open or Closed Side Vents

Figure 17a shows the average overpressure curves for the entire length of the thick LB/TS side wall section, excluding the closed side vents, for the low vent problem. The curve for net average pressure shows a long steady rise from 132.3 kPa (19.2 psi) at 70.6 ms to a peak of 593.3 kPa (86.1 psi) at 141.4 ms, then a decrease to 513.9 kPa (74.5 psi) by 186.4 ms. Thus, there is a relatively large average overpressure, well above the peak incident shock overpressure of 241.3 kPa (35.0 psi), in this region for an extended period.

Figure 17b shows a similar set of curves for the same side wall section, excluding open side vents, for the normal vent problem. Here, the net pressure curve shows the effects of the open USV and DSV, and the more open P-RWE, by showing a great relative reduction in the average overpressure as compared with that for the low vent problem. The peak net pressure for the normal vent problem is 218.7 kPa (31.7 psi) at 91.4 ms, with a value of 185.8 kPa (26.9 psi) at the 186.4 ms ending time.

VI. Test Station

Figure 18a shows the average overpressure in the normal cross-section of the LB/TS at the test station location for the low vent problem (at the 20.0 m point in this computation). The first value of 189.3 kPa (27.5 psi) at 70.6 ms is below the peak incident shock overpressure of 241.3 kPa (35.0 psi) of the decaying blast wave because, at the problem initiation, this point is 41.9575 m behind the shock front, so it is already exhibiting a considerable amount of decay in its flow parameters. Even though there is a strong reflected shock still traveling toward the test station at the ending time of 186.4 ms, there is as yet no disturbance from it evident at the test station. The overpressure at the test station at this time is 137.1 kPa (19.9 psi).

Figure 18b shows the average overpressure in the same test station cross-section for the normal vent problem. The curve is identical to that for the low vent problem shown in Figure 18a. Two reasonable conclusions that can be tentatively drawn from this are that neither a compression wave (in the low vent problem) nor an expansion wave (in the normal vent problem) from the exit region of the LB/TS has yet reached the test station.

VII. Conclusion

The results and observations discussed here are to be considered preliminary. It does appear that the combined RWE and side vent design analyzed here is efficient in its reduction of reflected compression and shock waves from the RWE's while minimizing the generation of excessively strong expansion waves. The loadings generated on the RWE's and the LB/TS side wall appear to be within ranges that allow practical designs, assuming that all vent areas are at their proper settings.

The low vent problem, embodying a worst-case assumption of the possible settings of

the areas of the USV, DSV, and P-RWE, combined with the strongest design blast wave, appears to generate blast loads on the RWE's that are beyond the reach of a reasonable, practical design. The loads on the LB/TS side wall may also be prohibitively large. It seems reasonable to design the LB/TS with a set of interlocks with logic that requires failure to a safe state such that the drivers cannot be pressurized, and the diaphragms (or throat valves) cannot be burst (opened) unless the RWE('s) and side vents (if any) are in their proper positions. It would also be prudent to have a design for the RWE('s) and any side vents such that they would fail to a fully open position to further assure the saving of the LB/TS in the event of an off-design firing.

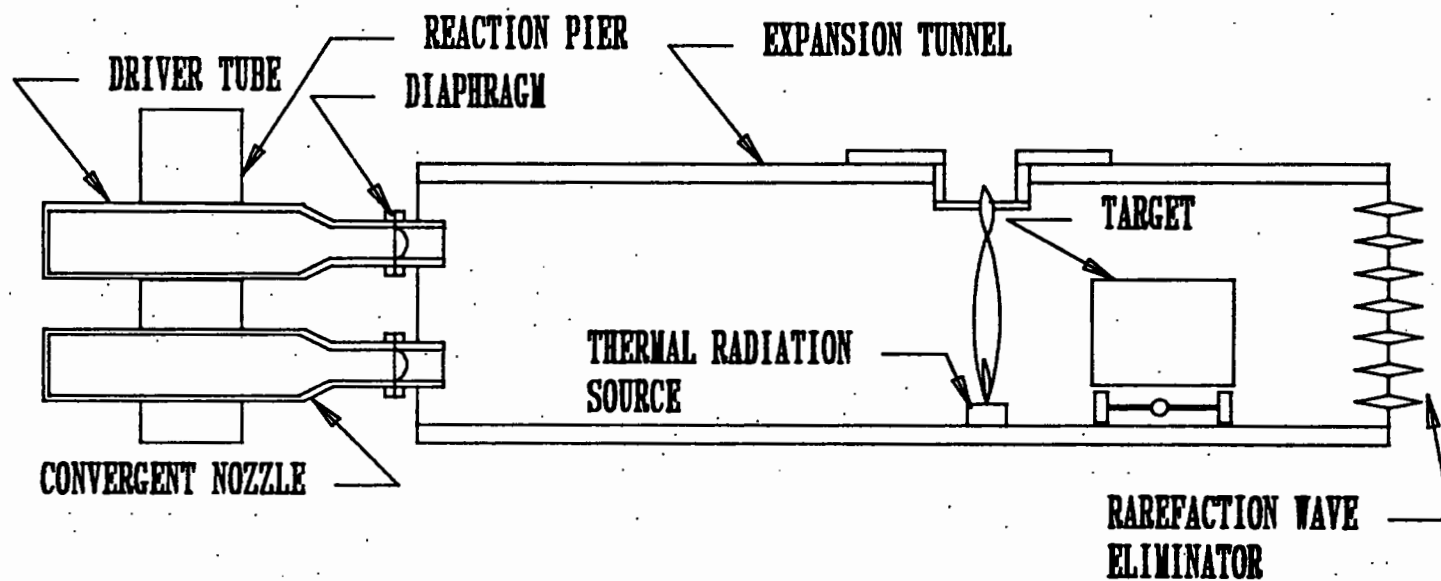


Figure 1a. A Simplified Schematic of the Proposed US LB/TS. (Courtesy of R. Pearson.)

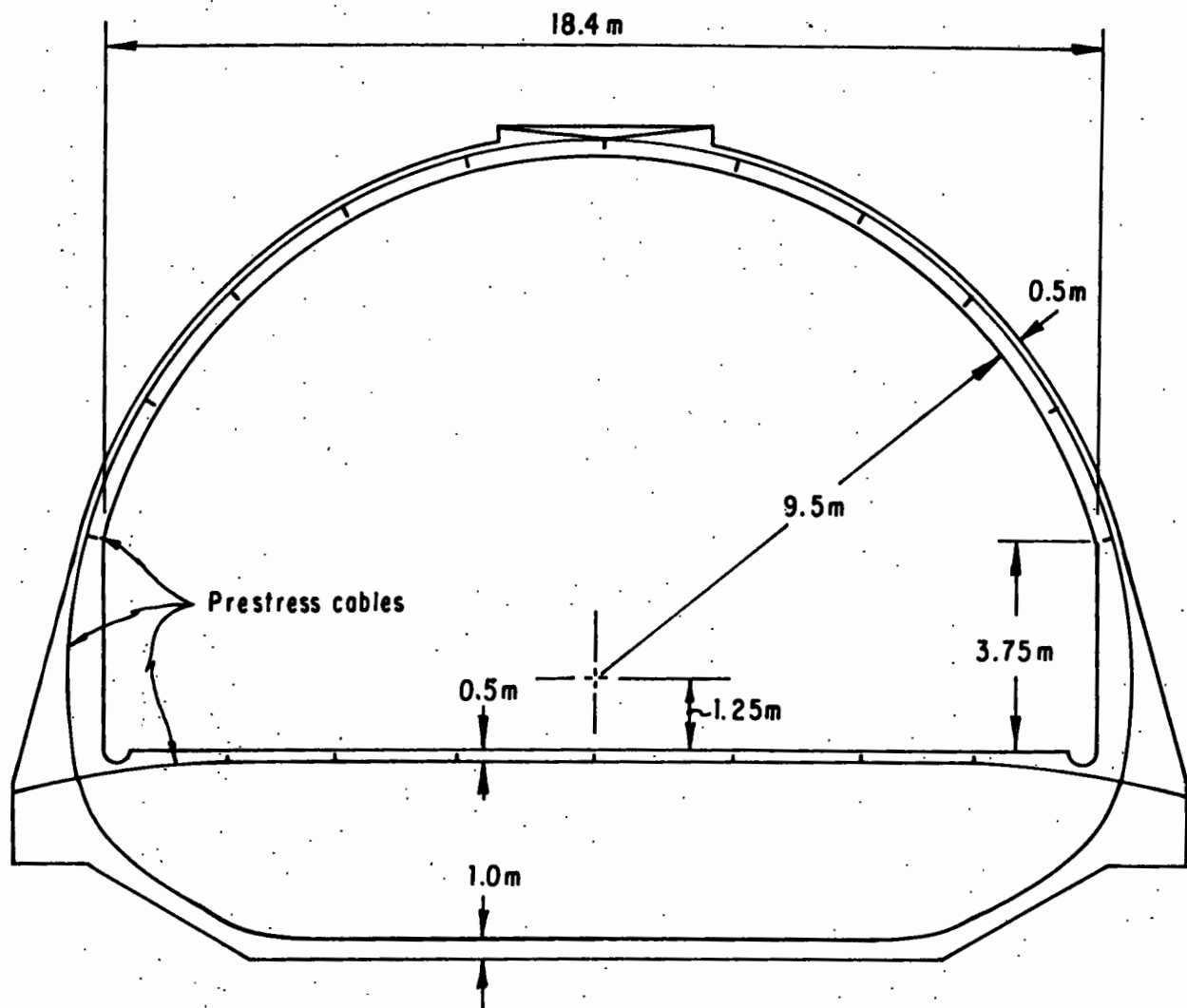


Figure 1b. Proposed LB/TS Cross-Section. (Courtesy of R. Pearson.)

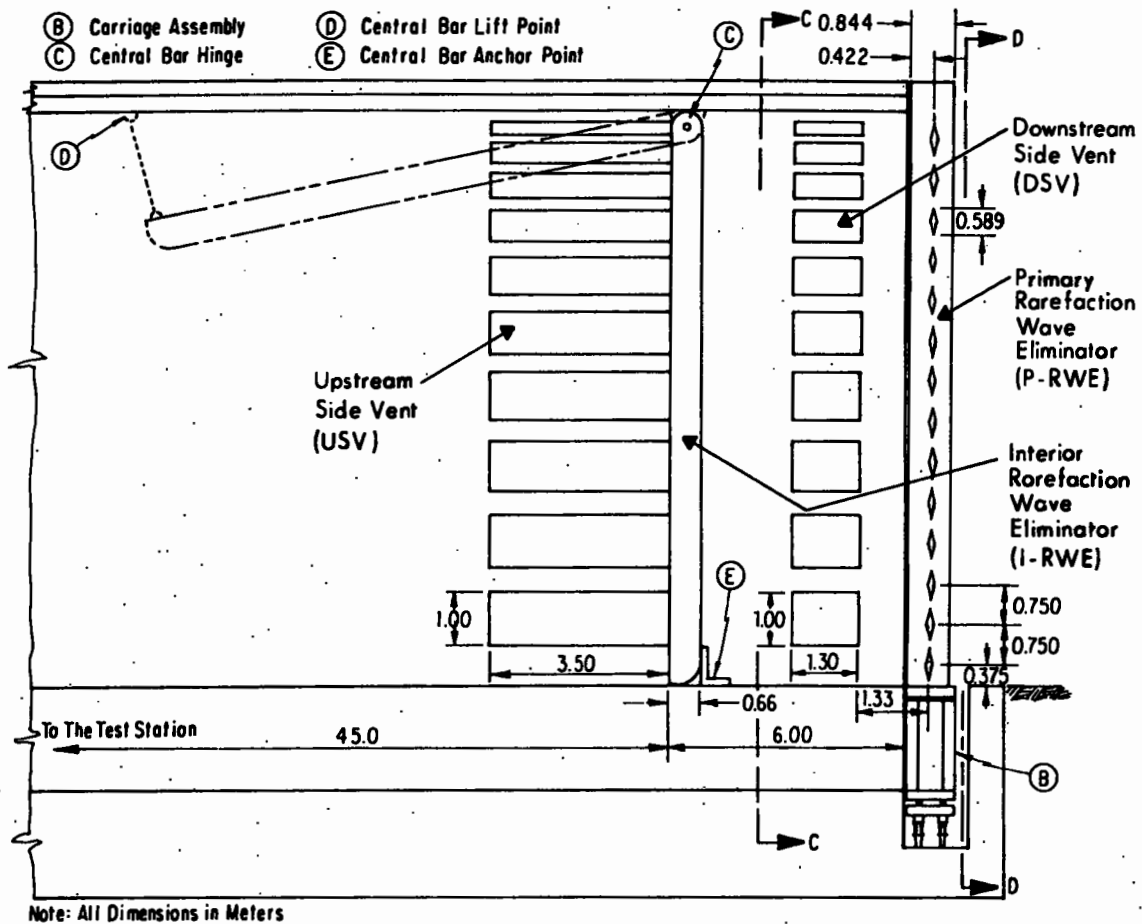


Figure 2. Axial Section through the Expansion Tunnel (Section A-A in Figure 3). (Courtesy of R. Pearson.)

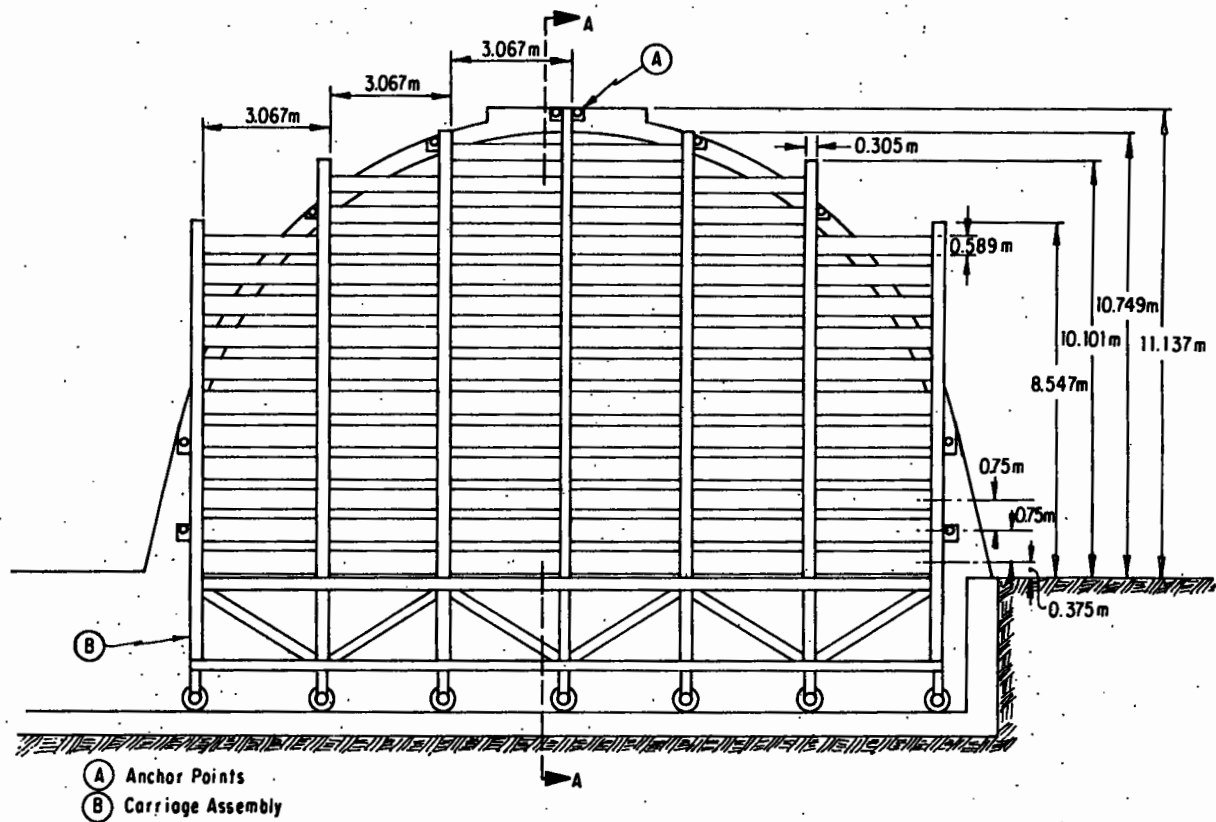


Figure 3. Exit Plane of the Primary Rarefaction Wave Eliminator (Section D-D in Figure 2). (Courtesy of R. Pearson.)

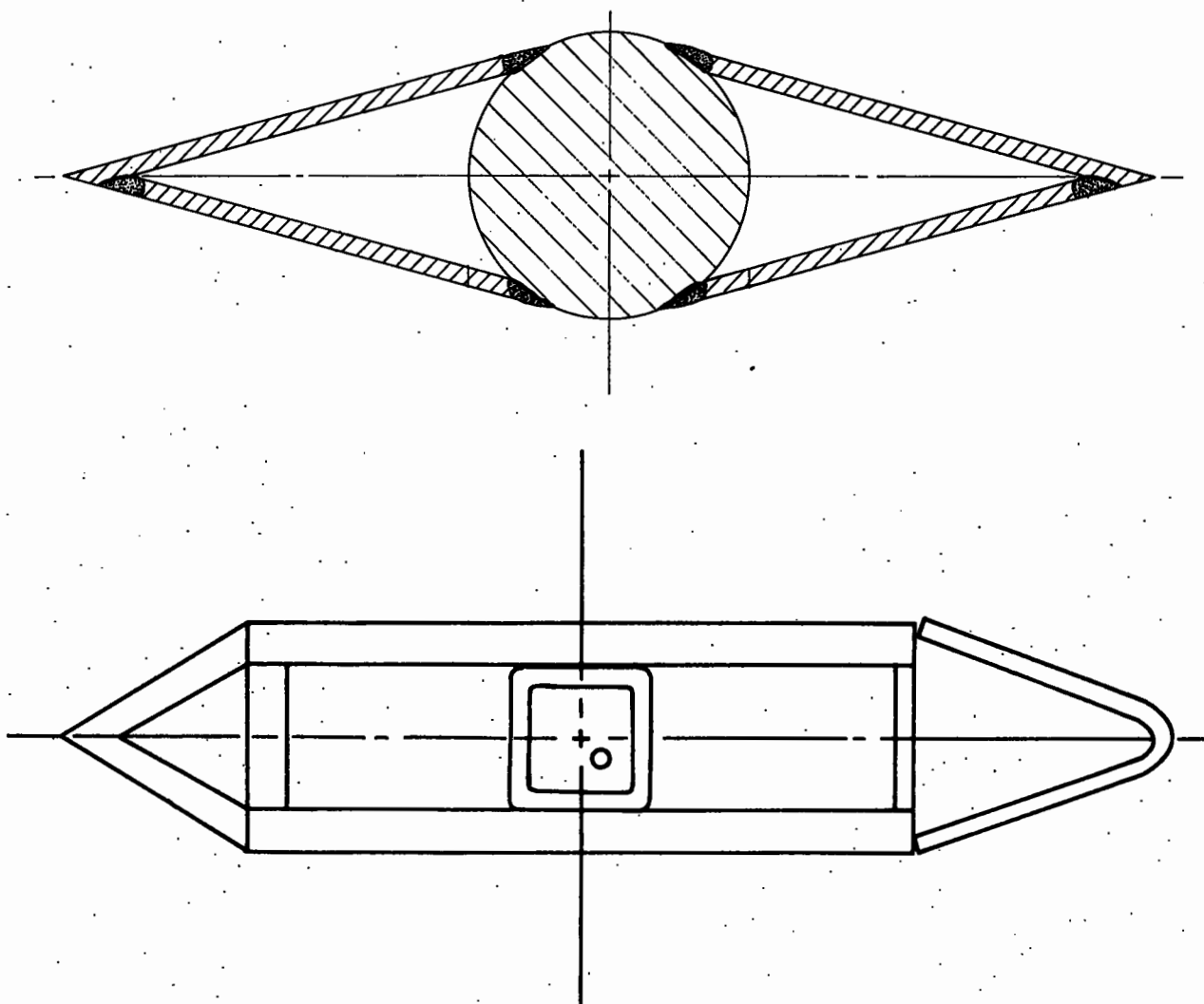


Figure 4. Two Candidate Shapes of the Vanes for the Primary Rarefaction Wave Eliminator.

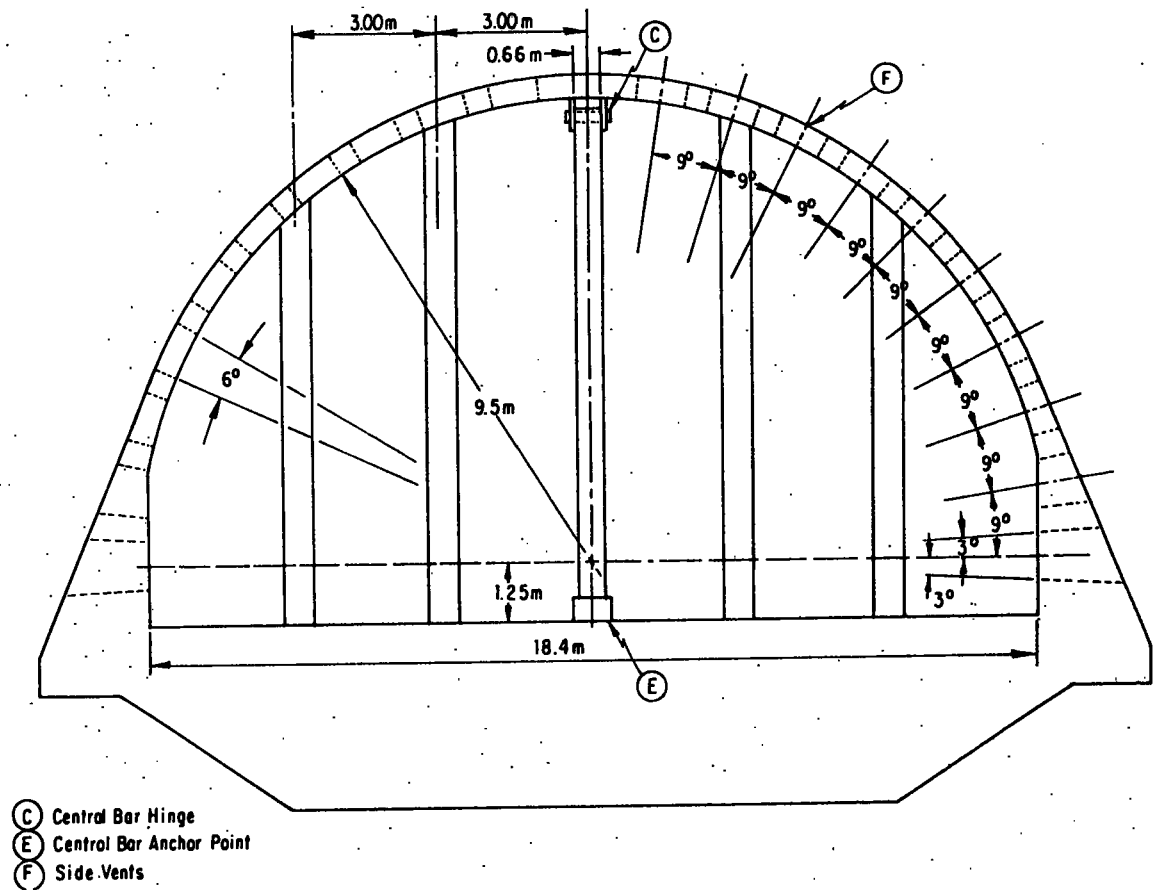


Figure 5. Tunnel Cross Section Looking Upstream at the Interior Rarefaction Wave Eliminator (Section C-C in Figure 2). (Courtesy of R. Pearson.)

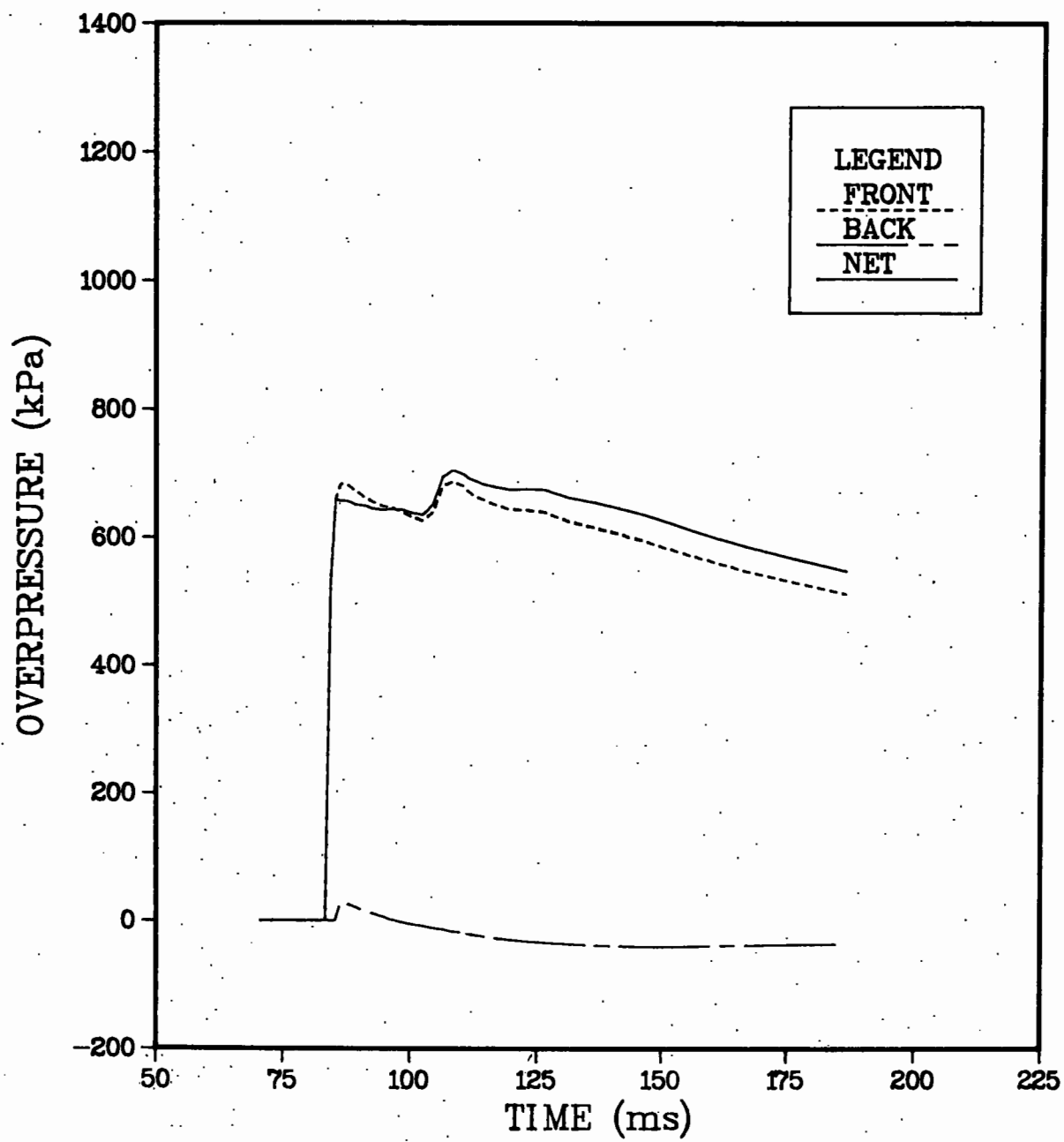


Figure 6a. Average Overpressure on the P-RWE, Low Vent.

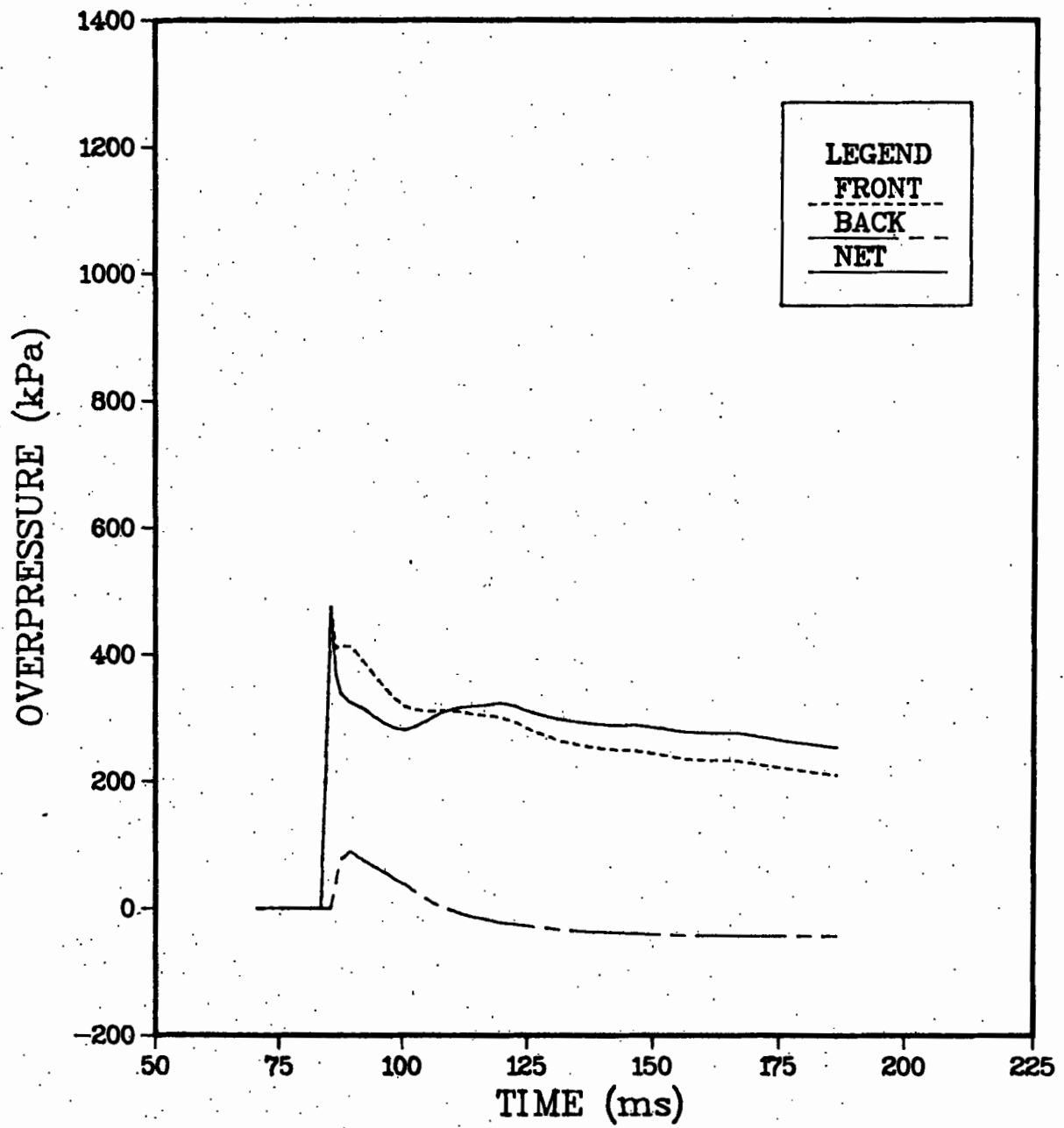


Figure 6b. Average Overpressure on the P-RWE, Normal Vent.

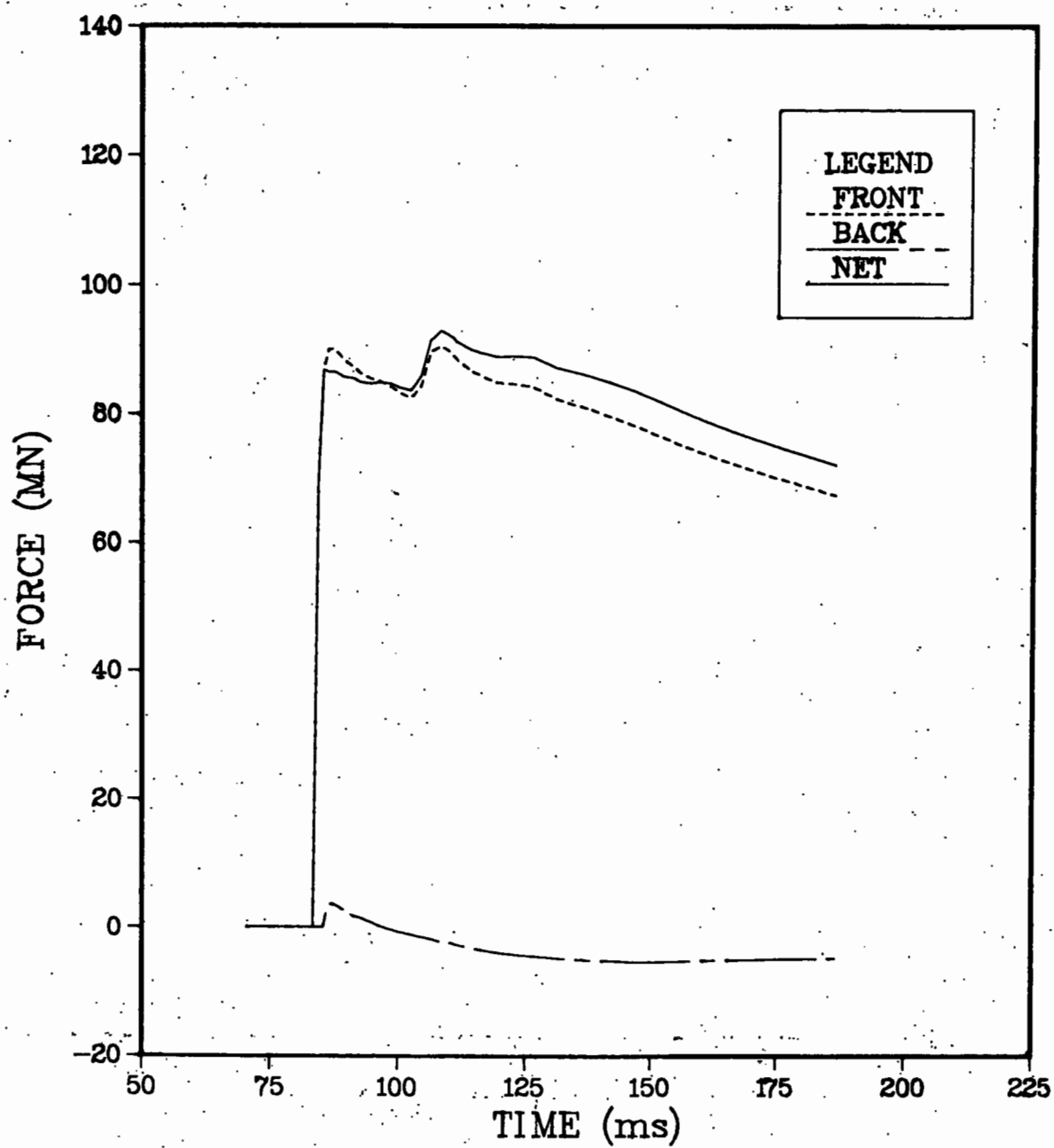


Figure 7a. Axial Forces on the P-RWE, Low Vent.

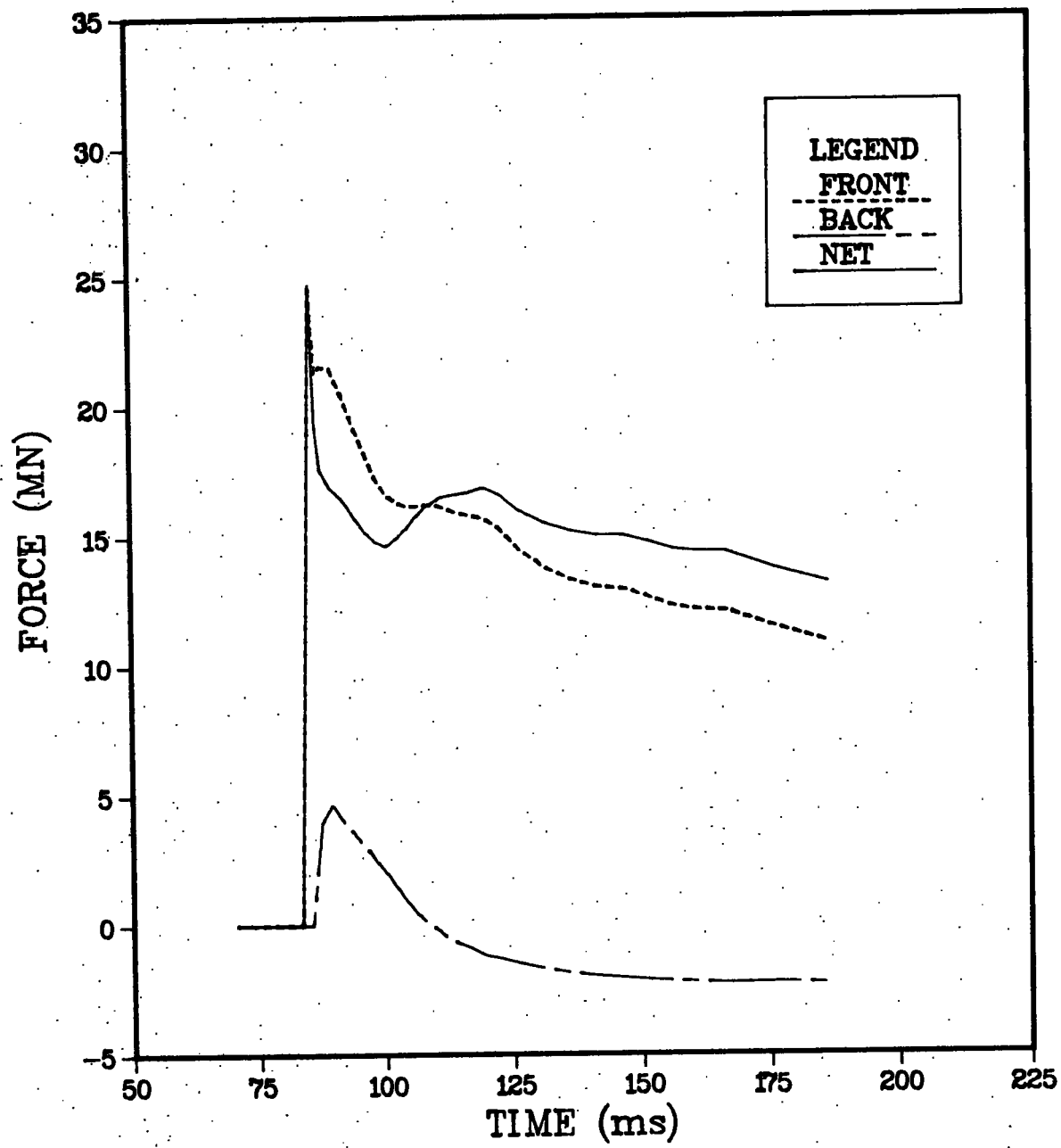


Figure 7b. Axial Forces on the P-RWE, Normal Vent.

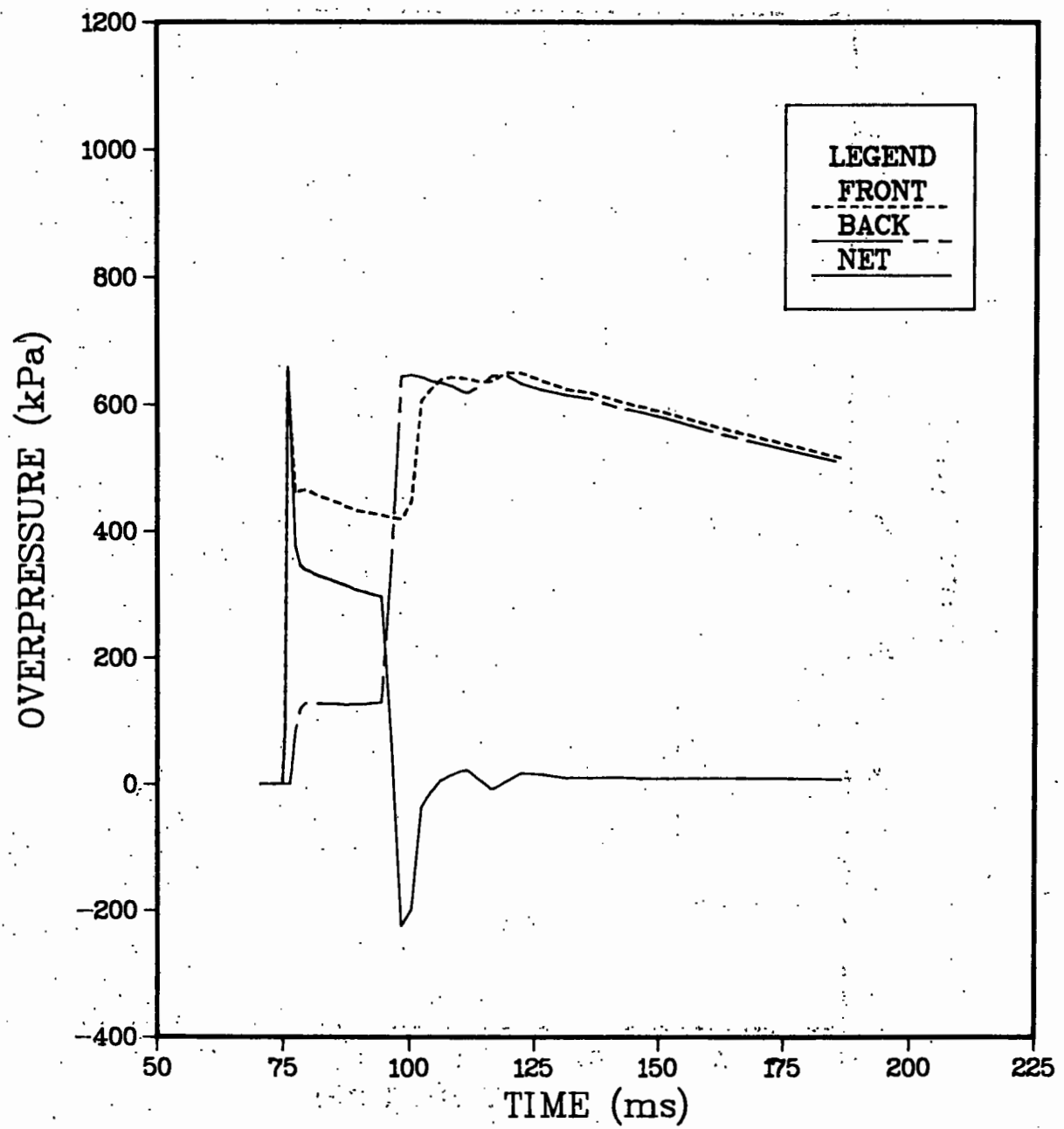


Figure 8a. Average Overpressure on the I-RWE, Low Vent.

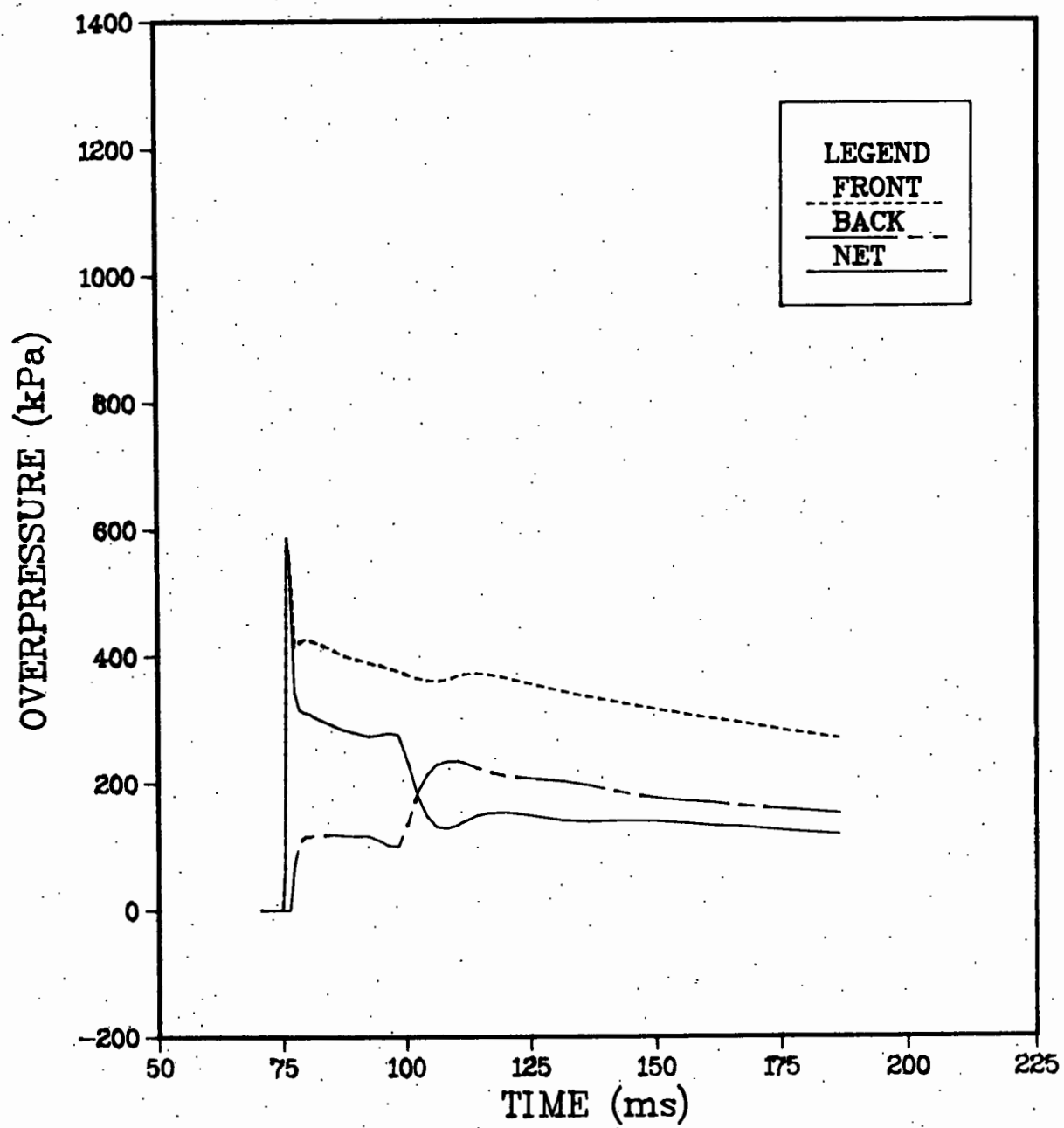
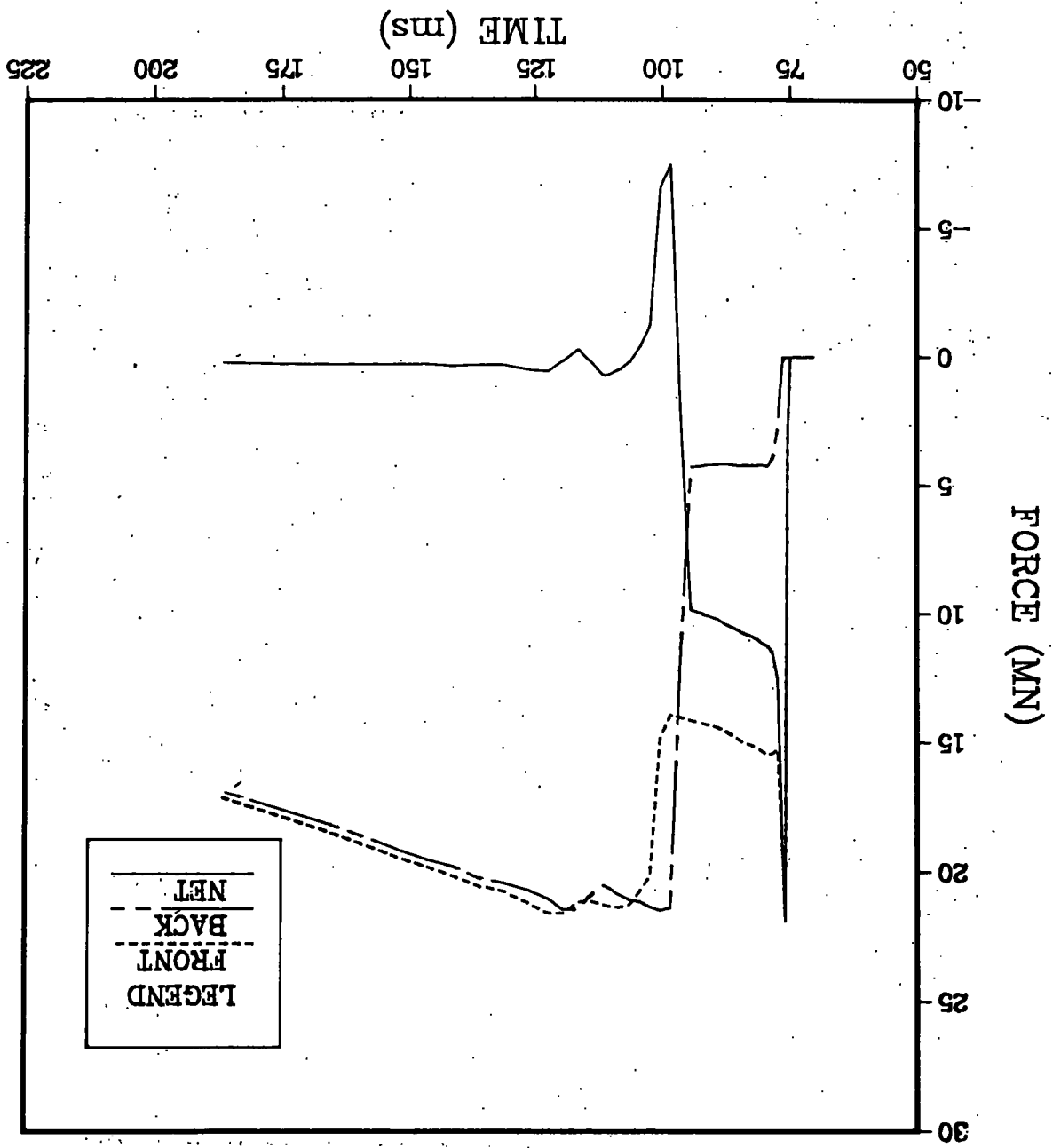


Figure 8b. Average Overpressure on the I-RWE, Normal Vent.

Figure 9a. Axial Forces on the I-RWE, Low Vent.



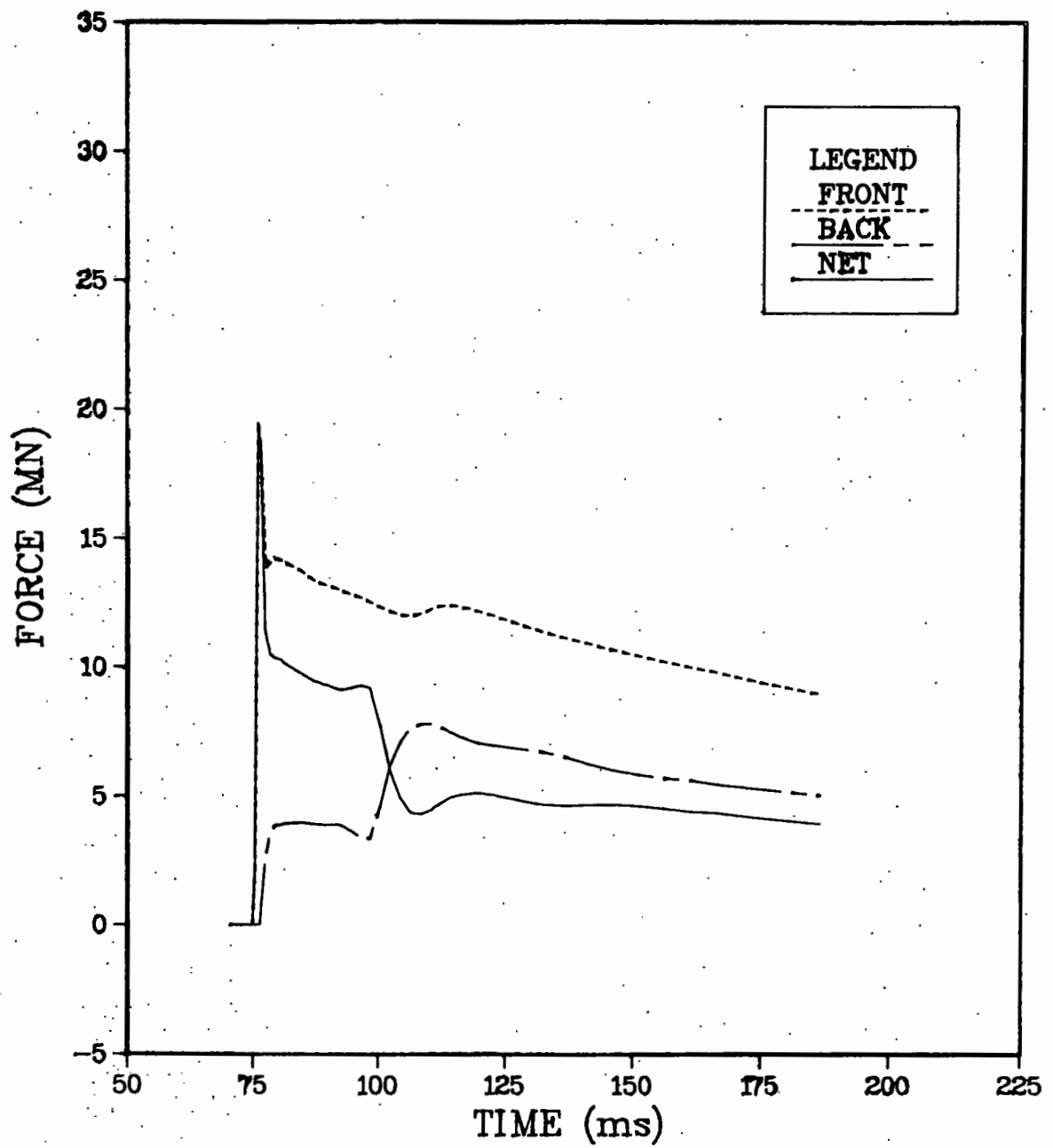


Figure 9b. Axial Forces on the I-RWE; Normal Vent.

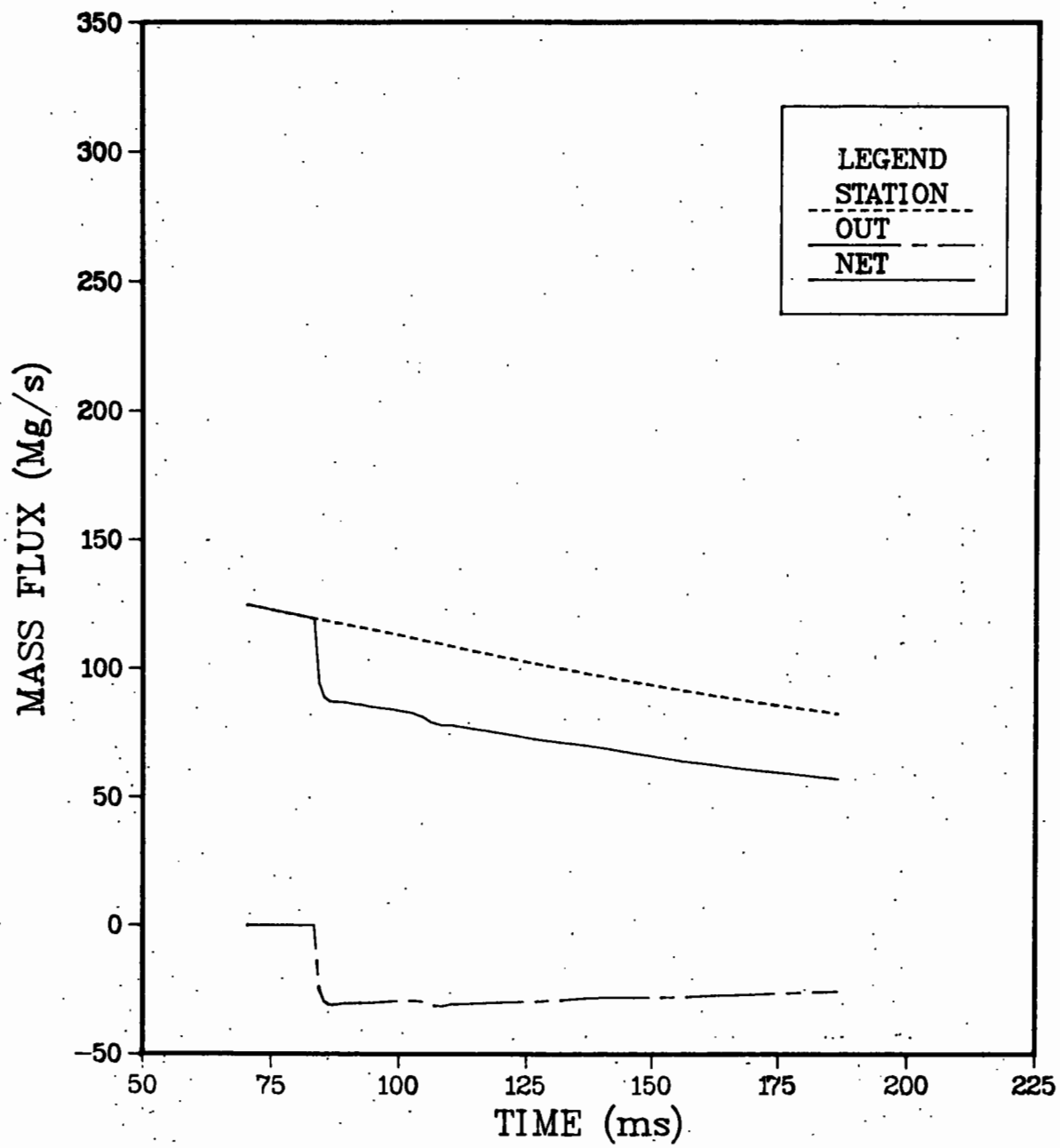


Figure 10a. Mass Flux in the LB/TS as a Control Volume, Low Vent.

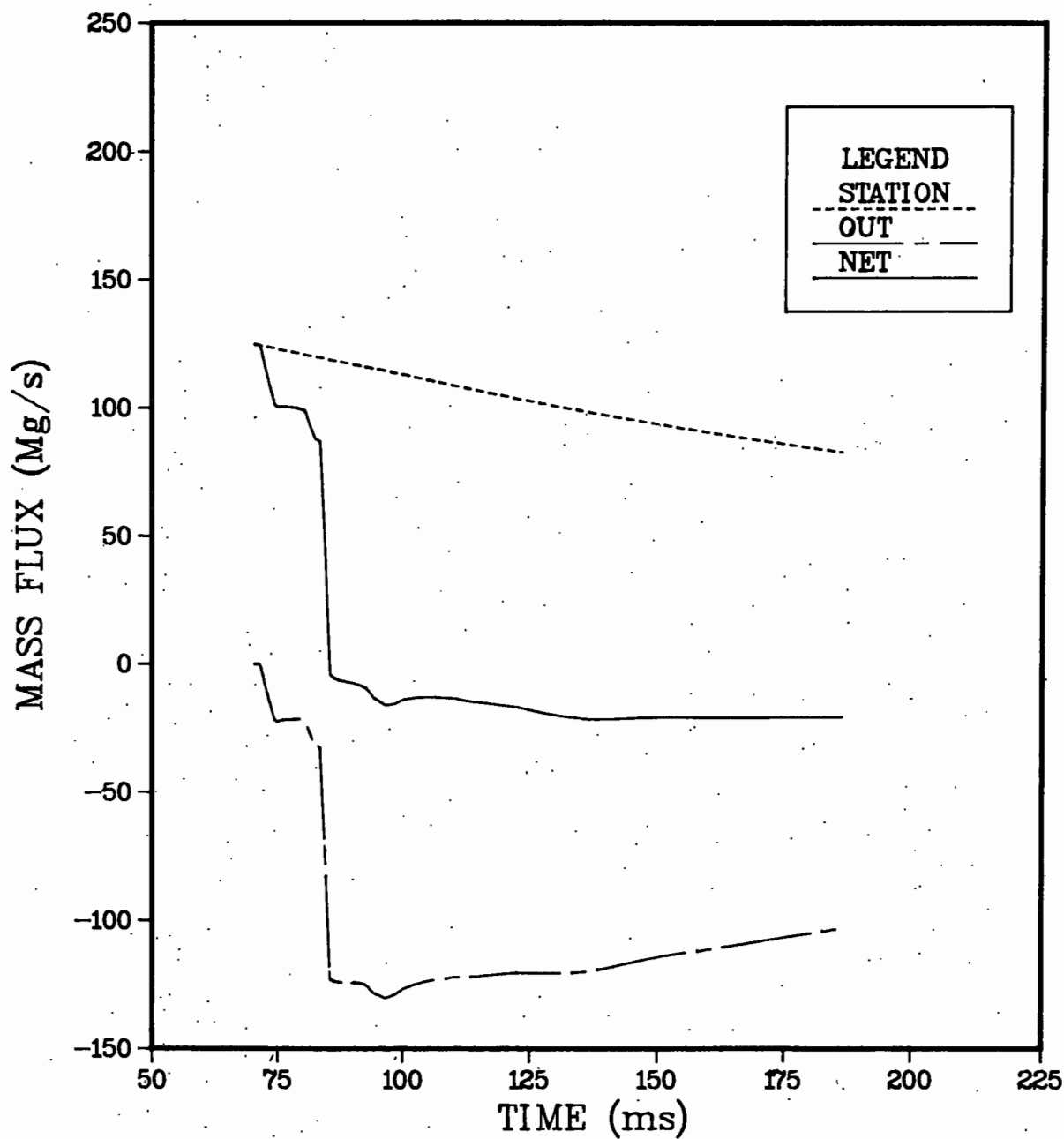


Figure 10b. Mass Flux in the LB/TS as a Control Volume, Normal Vent.

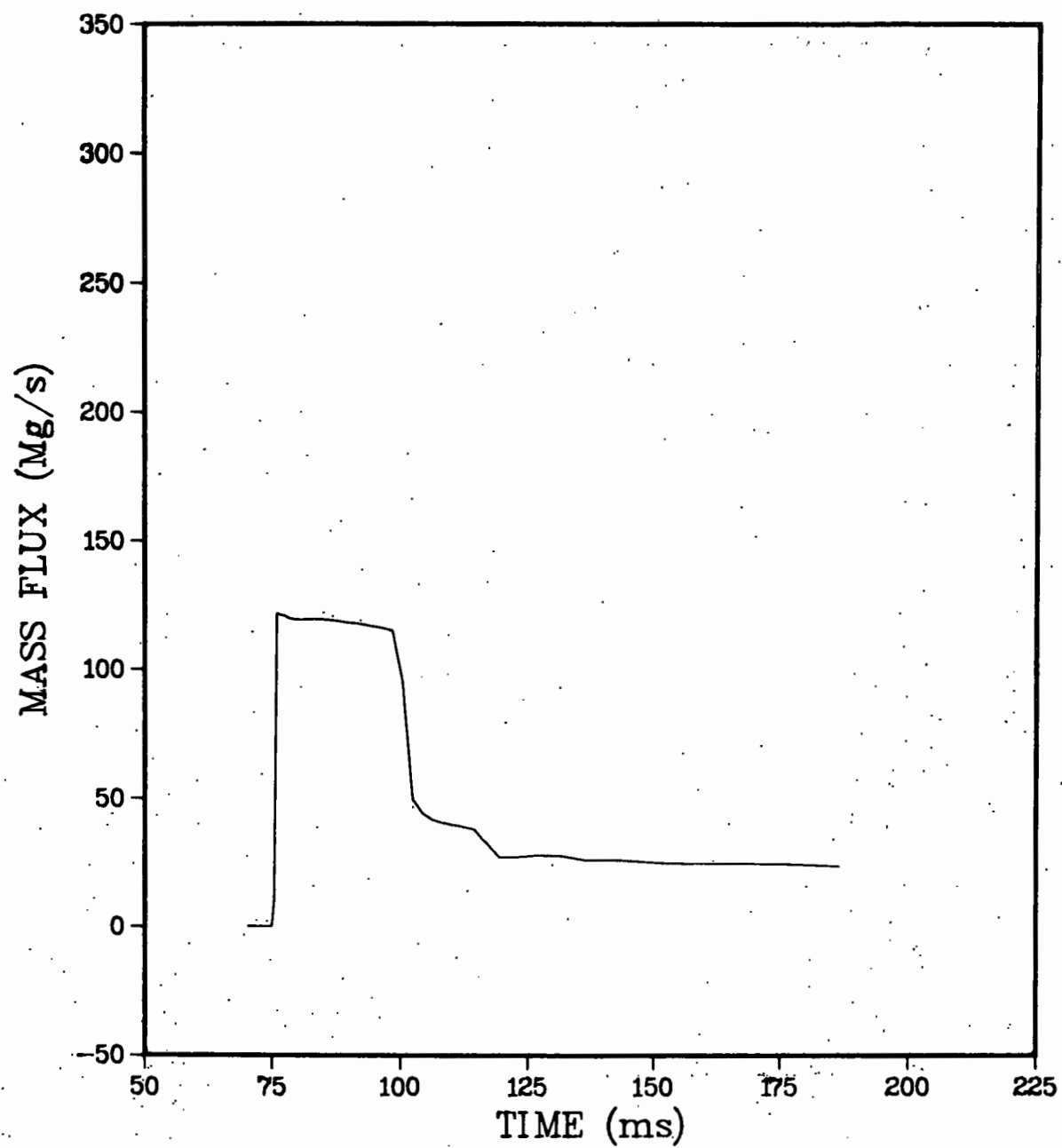


Figure 11a. Mass Flux through the I-RWE, Low Vent.

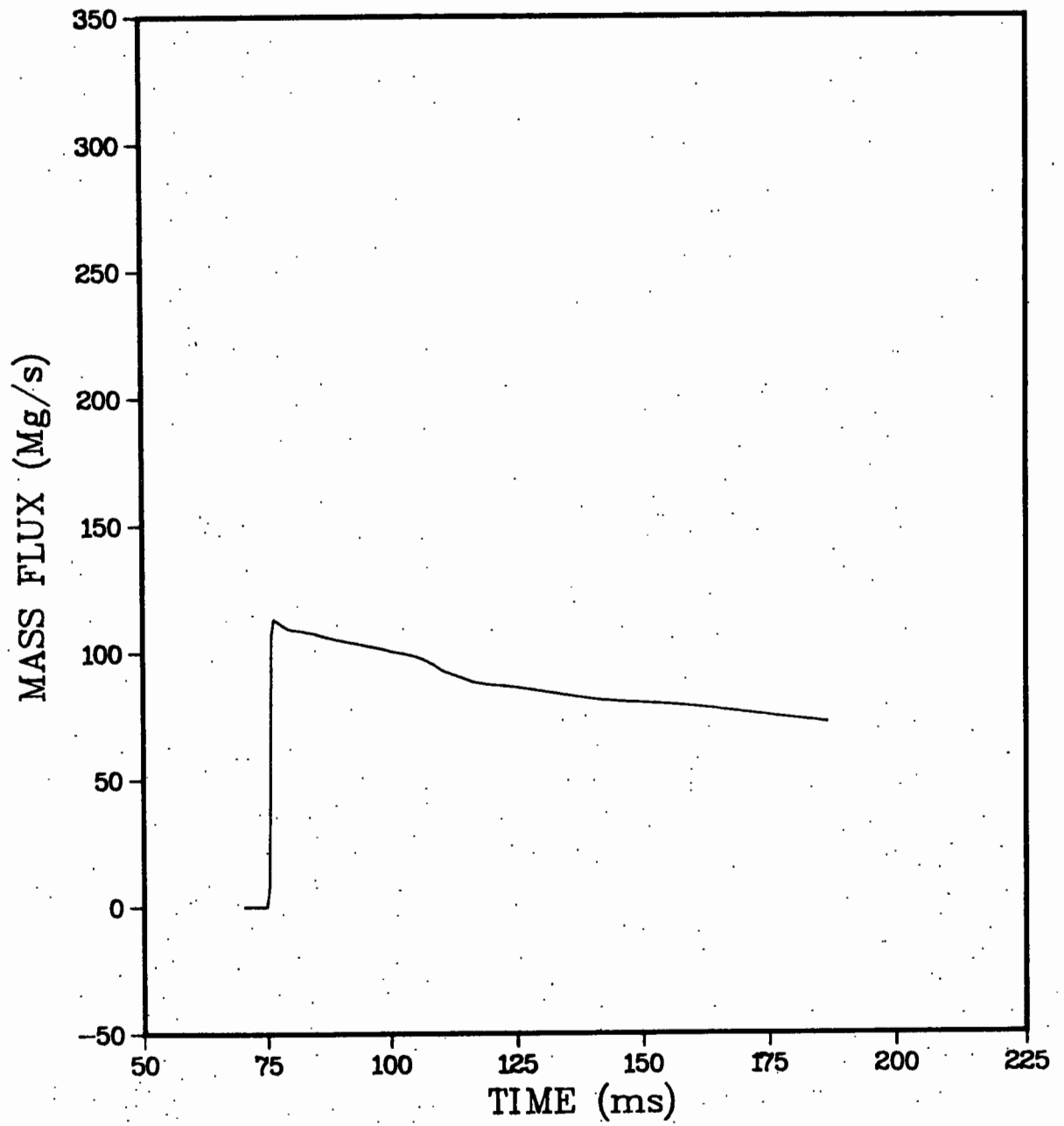


Figure 11b. Mass Flux through the I-RWE, Normal Vent.

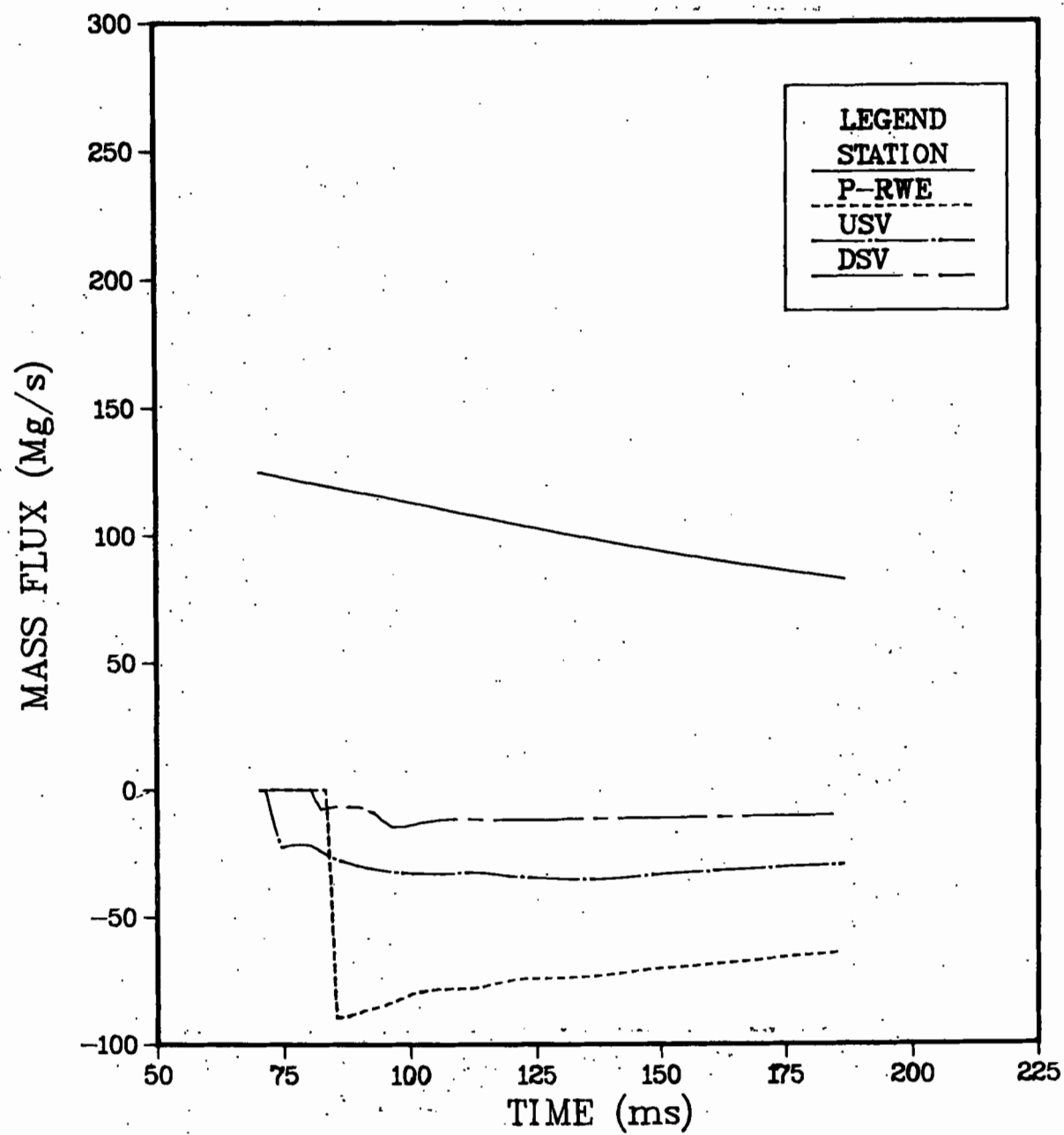


Figure 12. Mass Fluxes for Each Flow Area, Normal Vent.

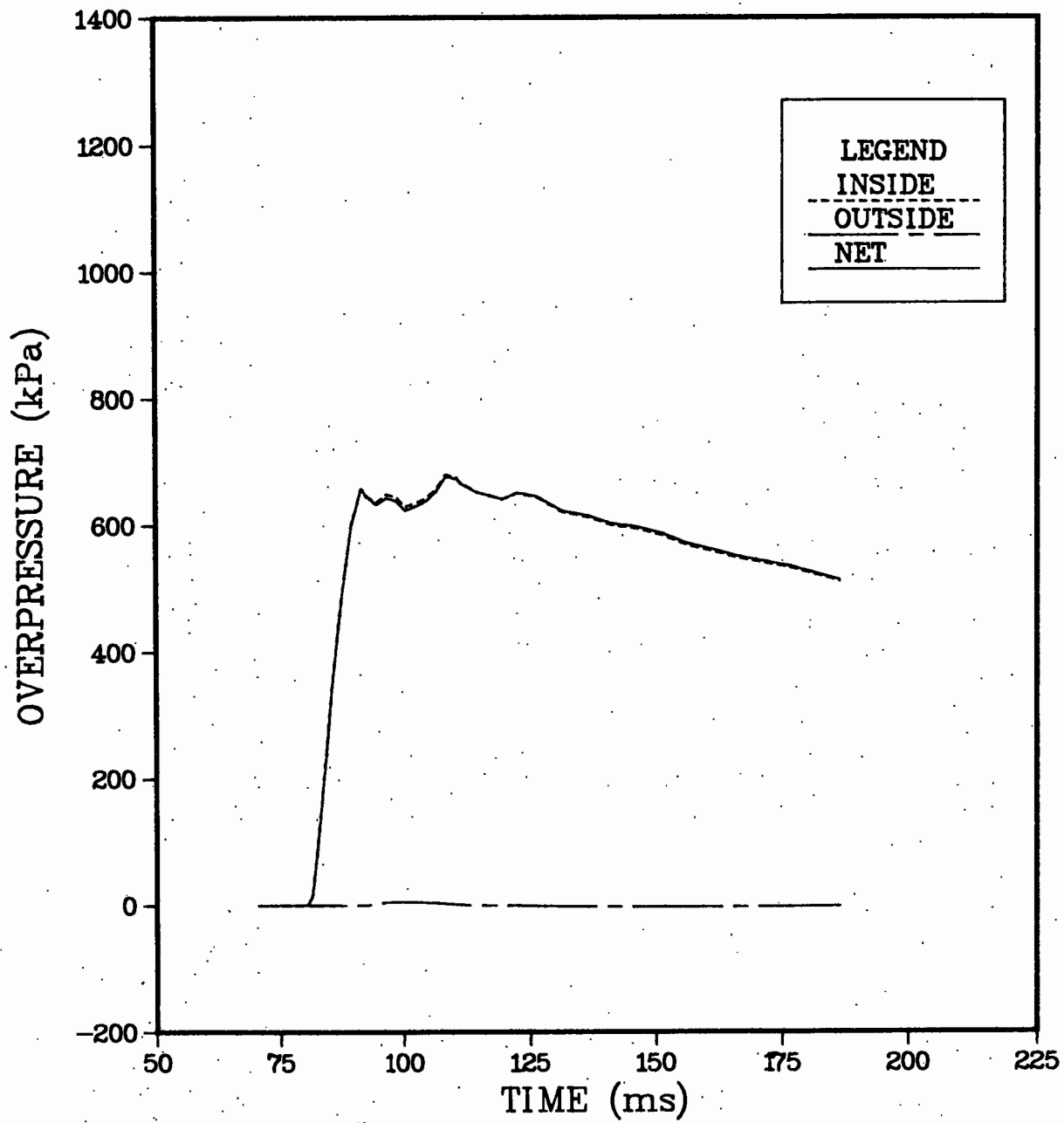


Figure 13a. Average Overpressure on the LB/TS Side Wall between the DSV and the P-RWE, Low Vent.

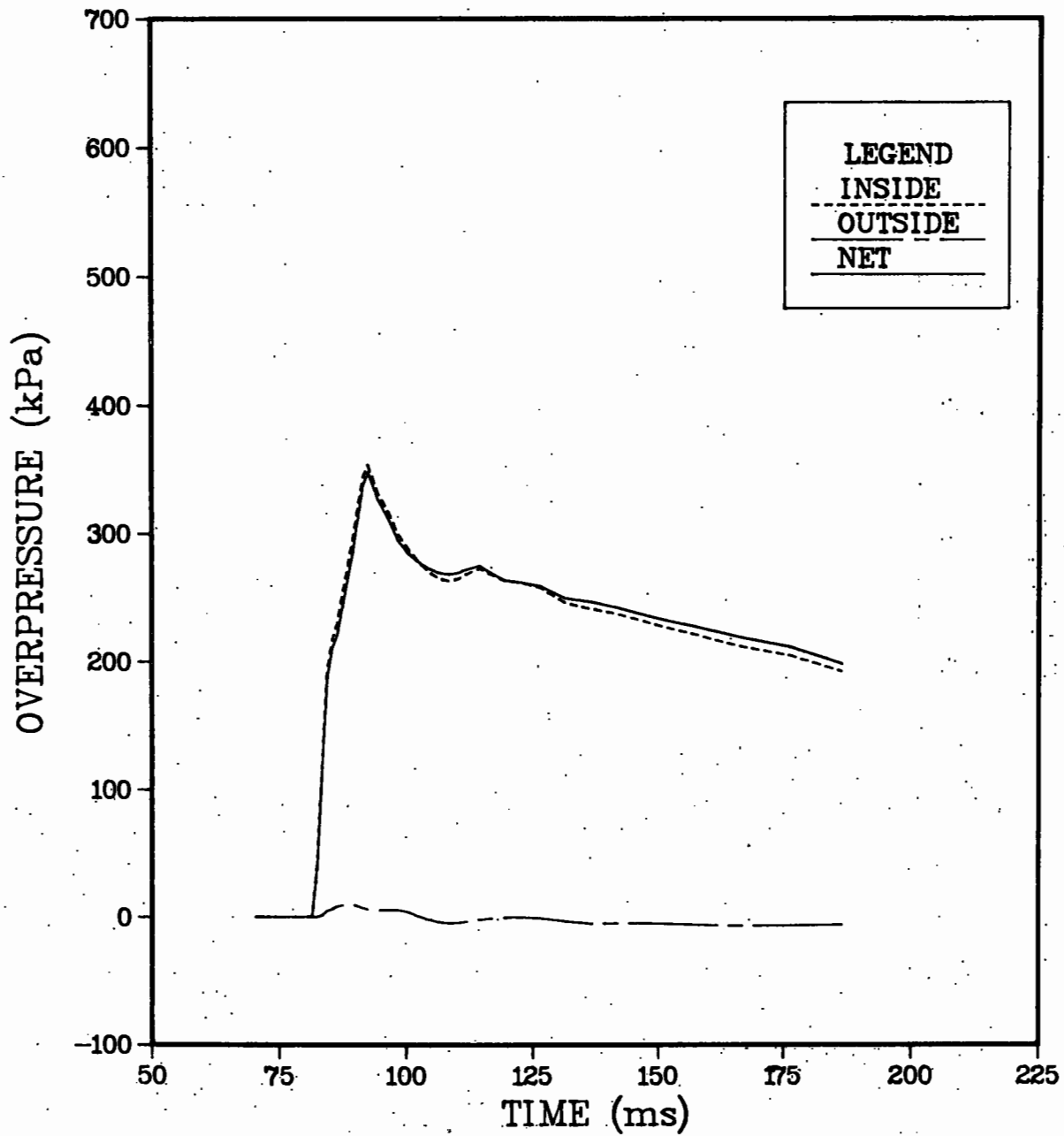


Figure 13b. Average Overpressure on the LB/TS Side Wall between the DSV and the P-RWE, Normal Vent.

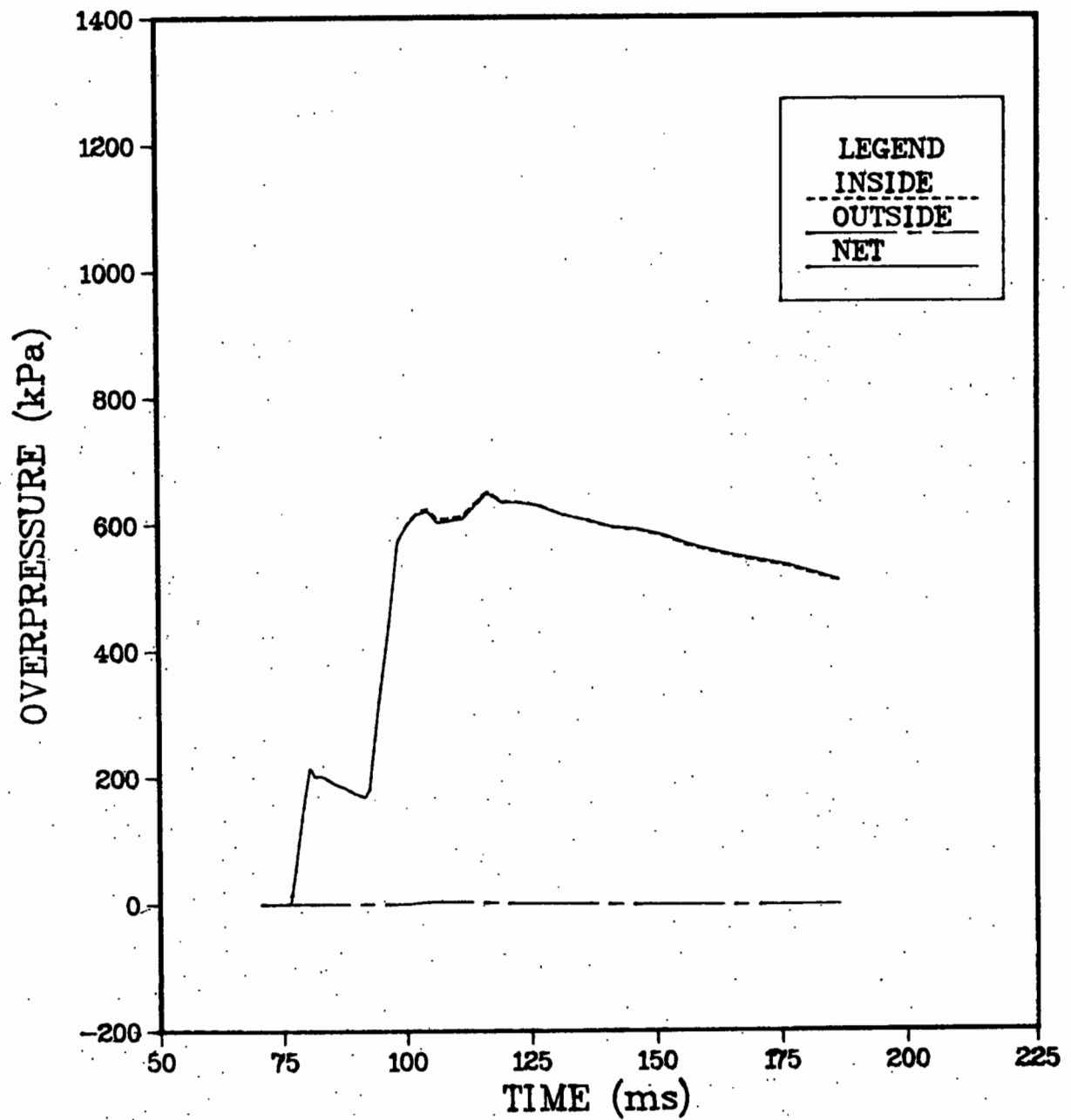


Figure 14a. Average Overpressure on the LB/TS Side Wall between the I-RWE and the DSV, Low Vent.

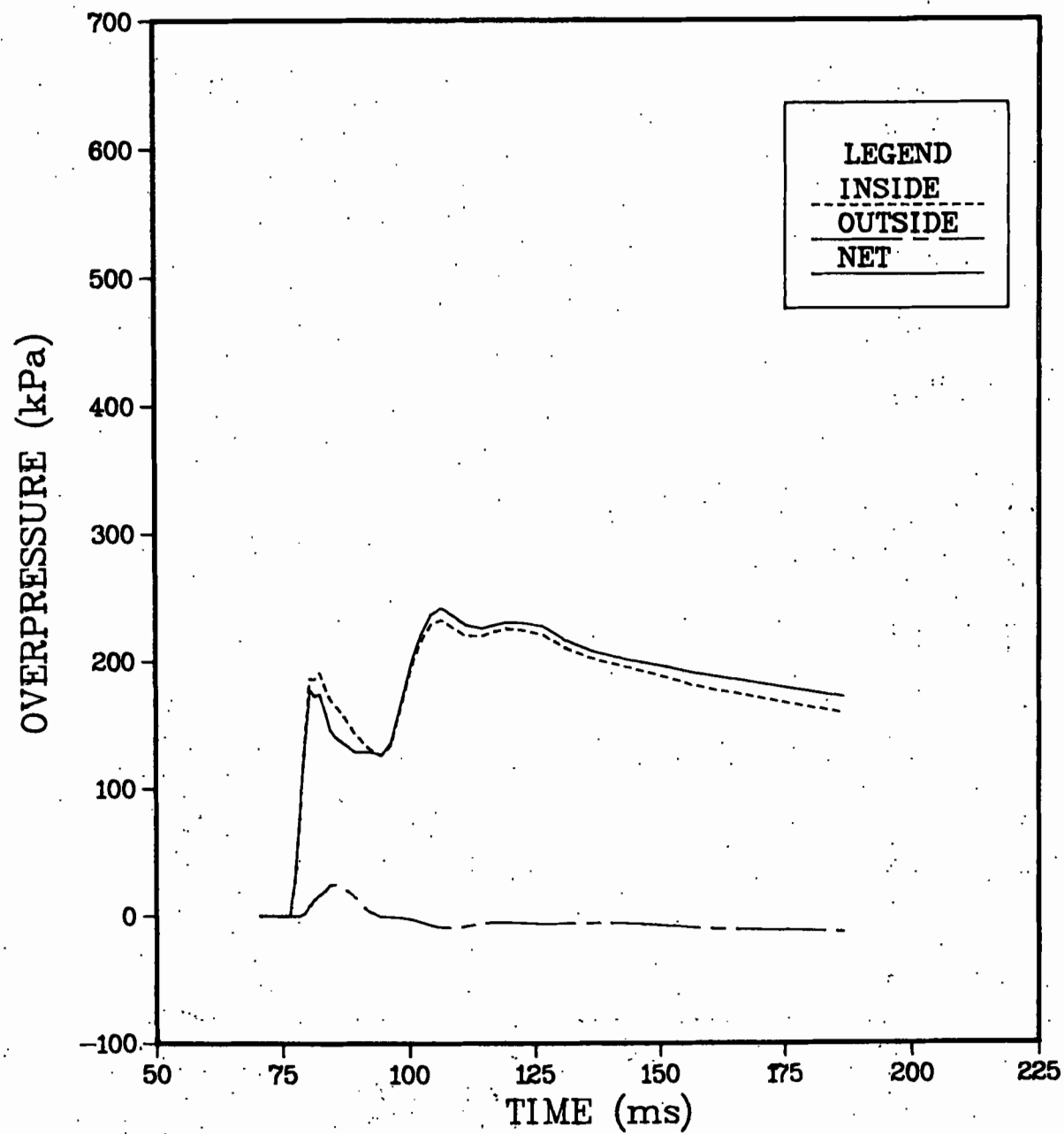


Figure 14b. Average Overpressure on the LB/TS Side Wall between the I-RWE and the DSV, Normal Vent.

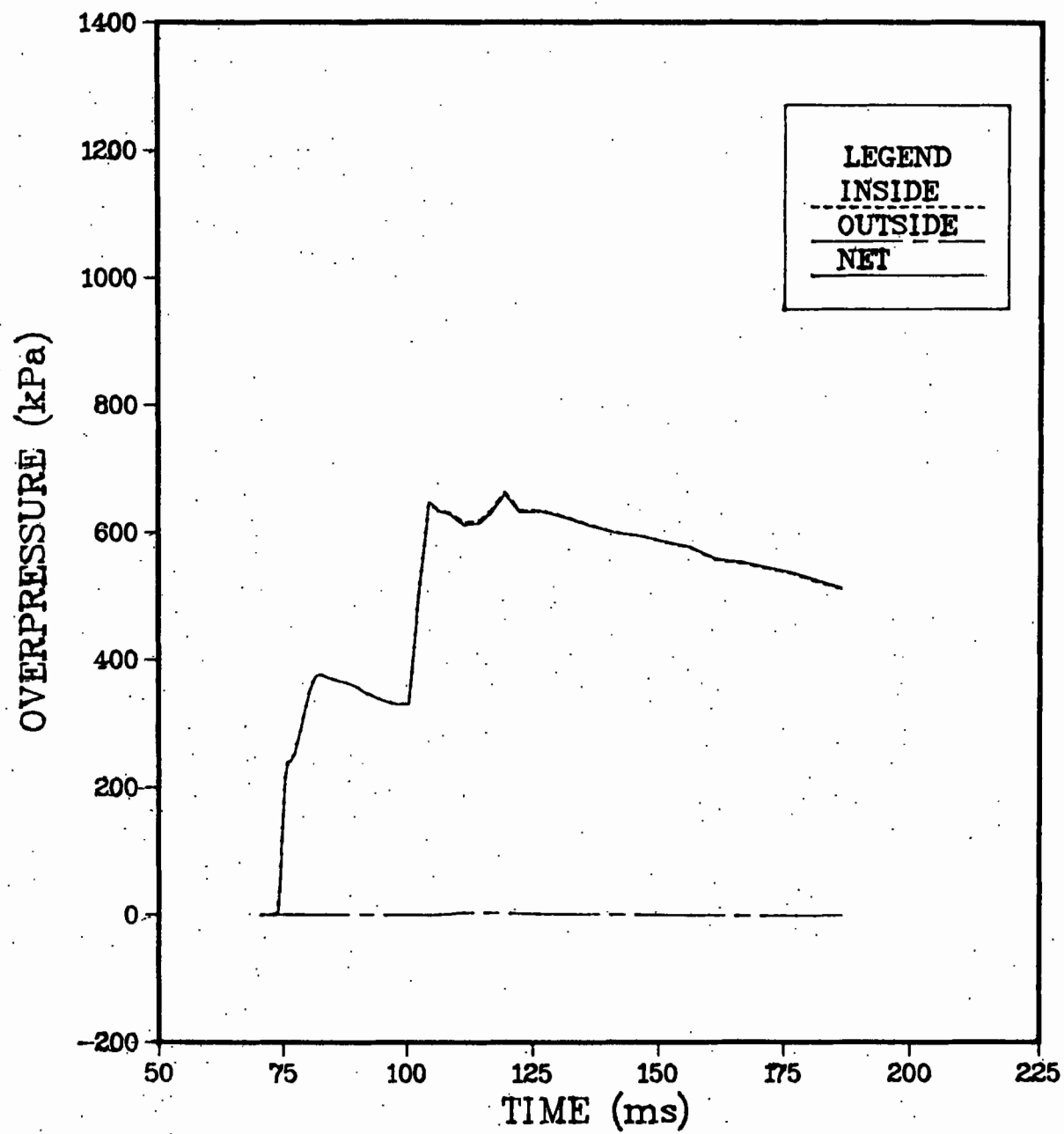


Figure 15a. Average Overpressure on the LB/TS Side Wall between the USV and the I-RWE, Low Vent.

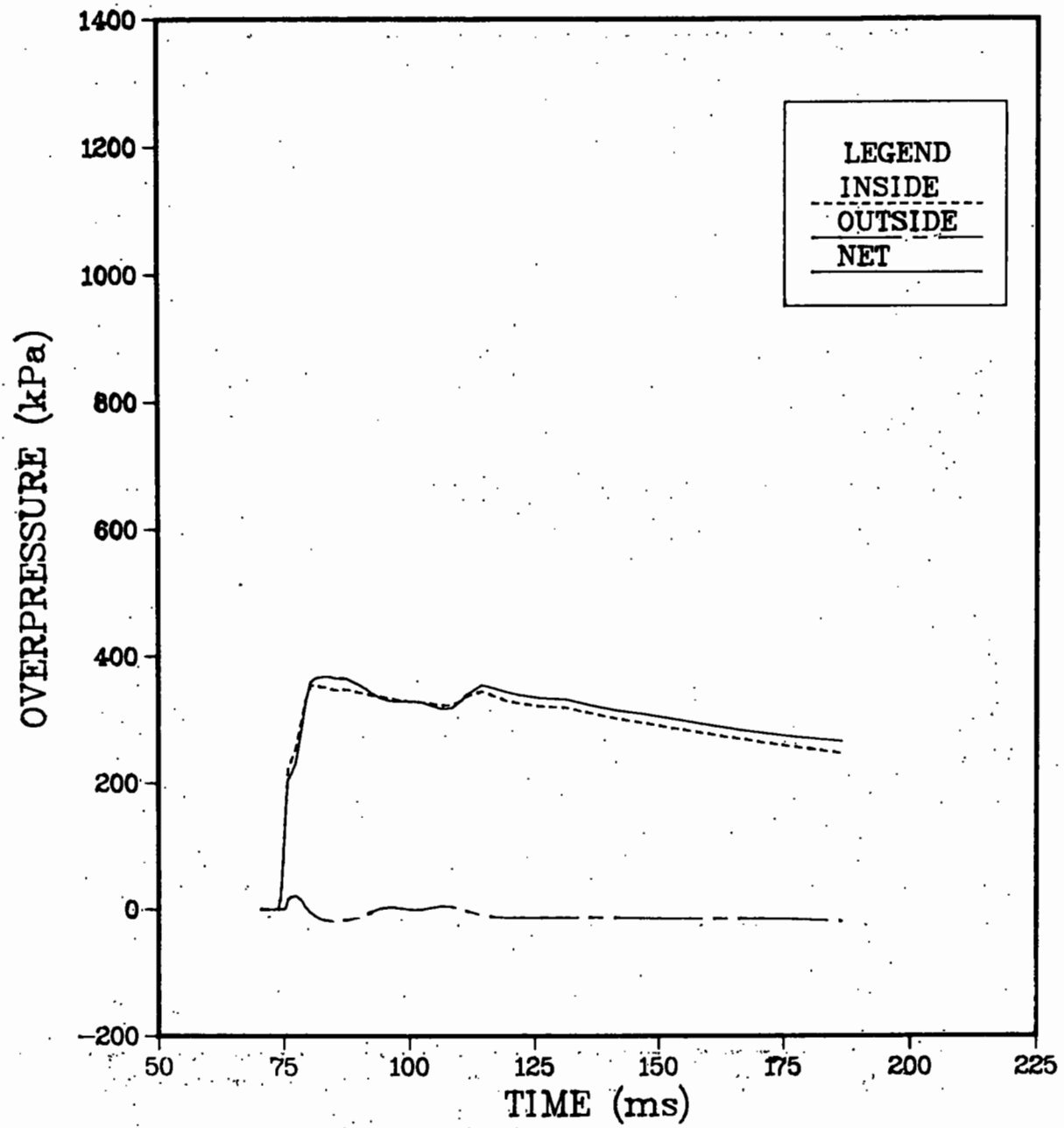


Figure 15b. Average Overpressure on the LB/TS Side Wall between the USV and the I-RWE, Normal Vent.

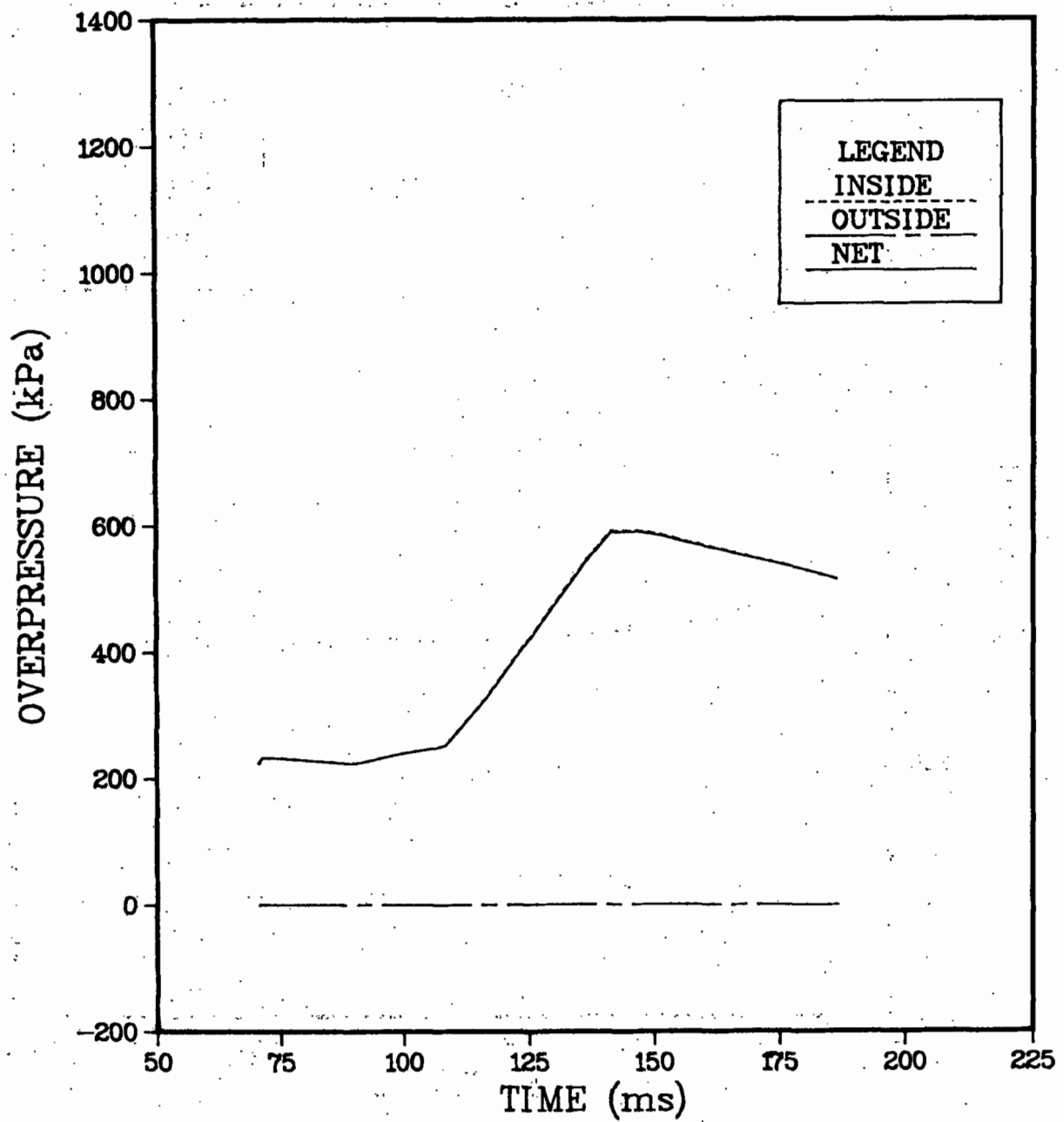


Figure 16a. Average Overpressure on the LB/TS Side Wall from the Start of the Thick Wall Section to the USV, Low Vent.

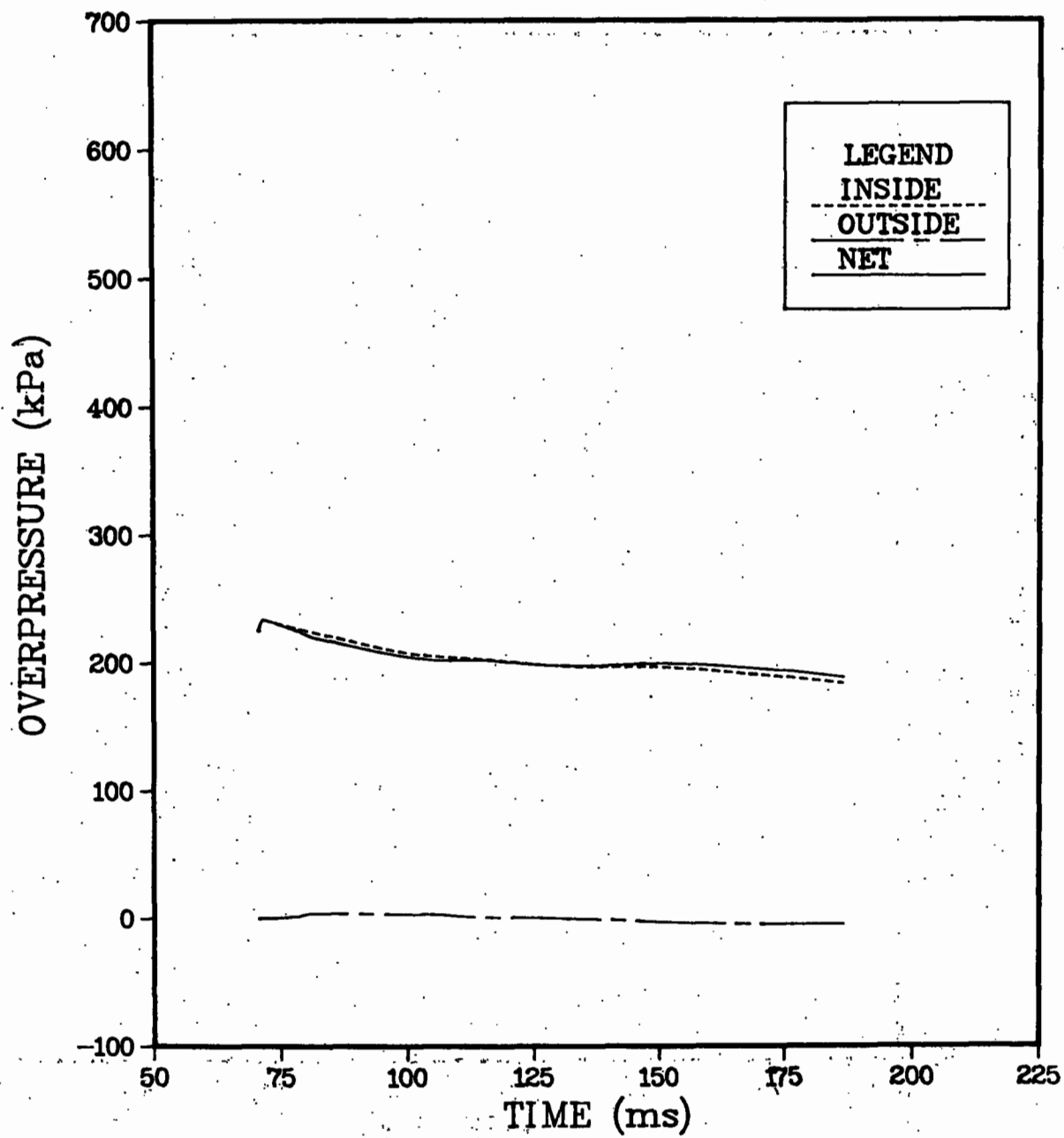


Figure 16b. Average Overpressure on the LB/TS Side Wall from the Start of the Thick Wall Section to the USV, Normal Vent.

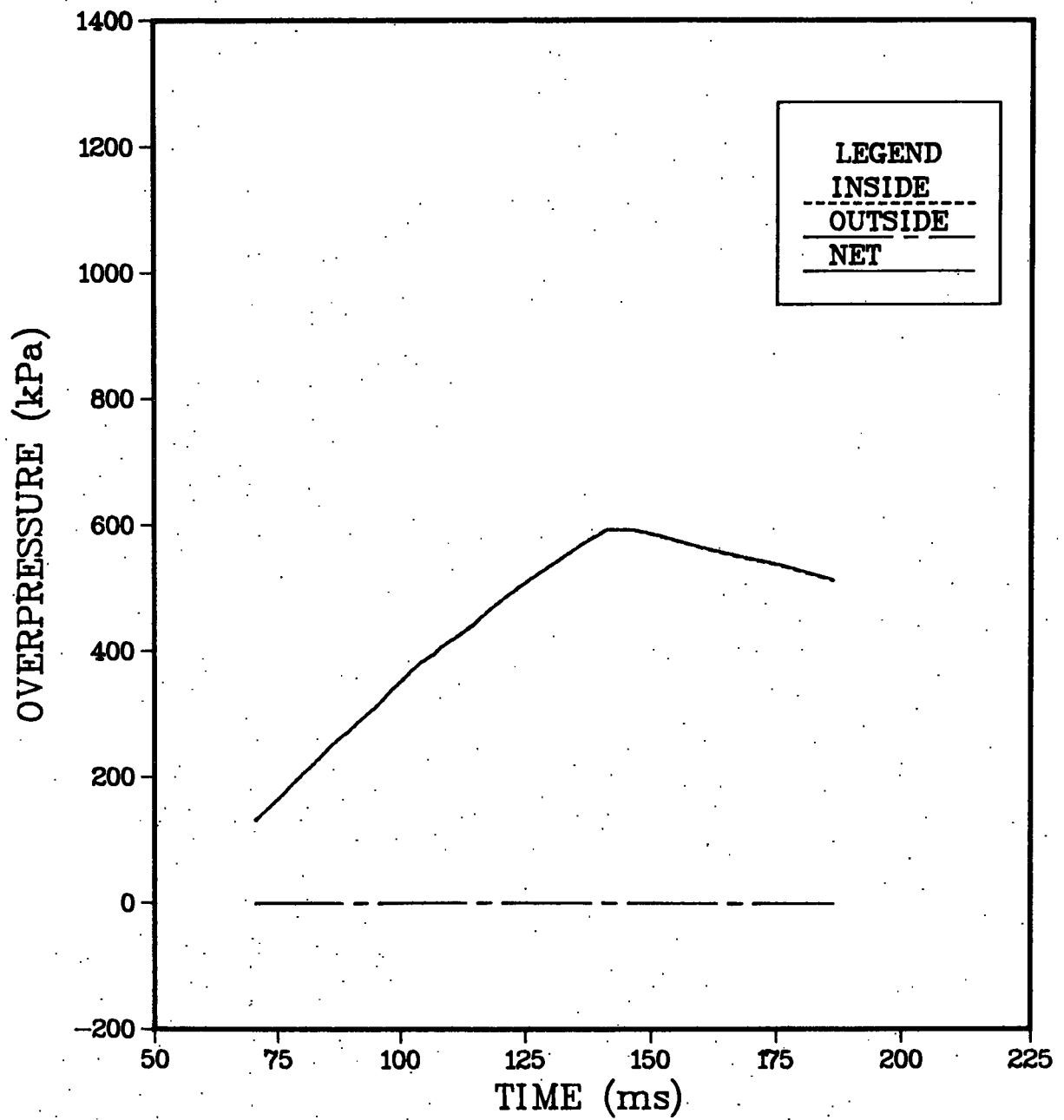


Figure 17a. Average Overpressure on the LB/TS Thick Side Wall Section, Excluding Closed Side Vent Areas, Low Vent.

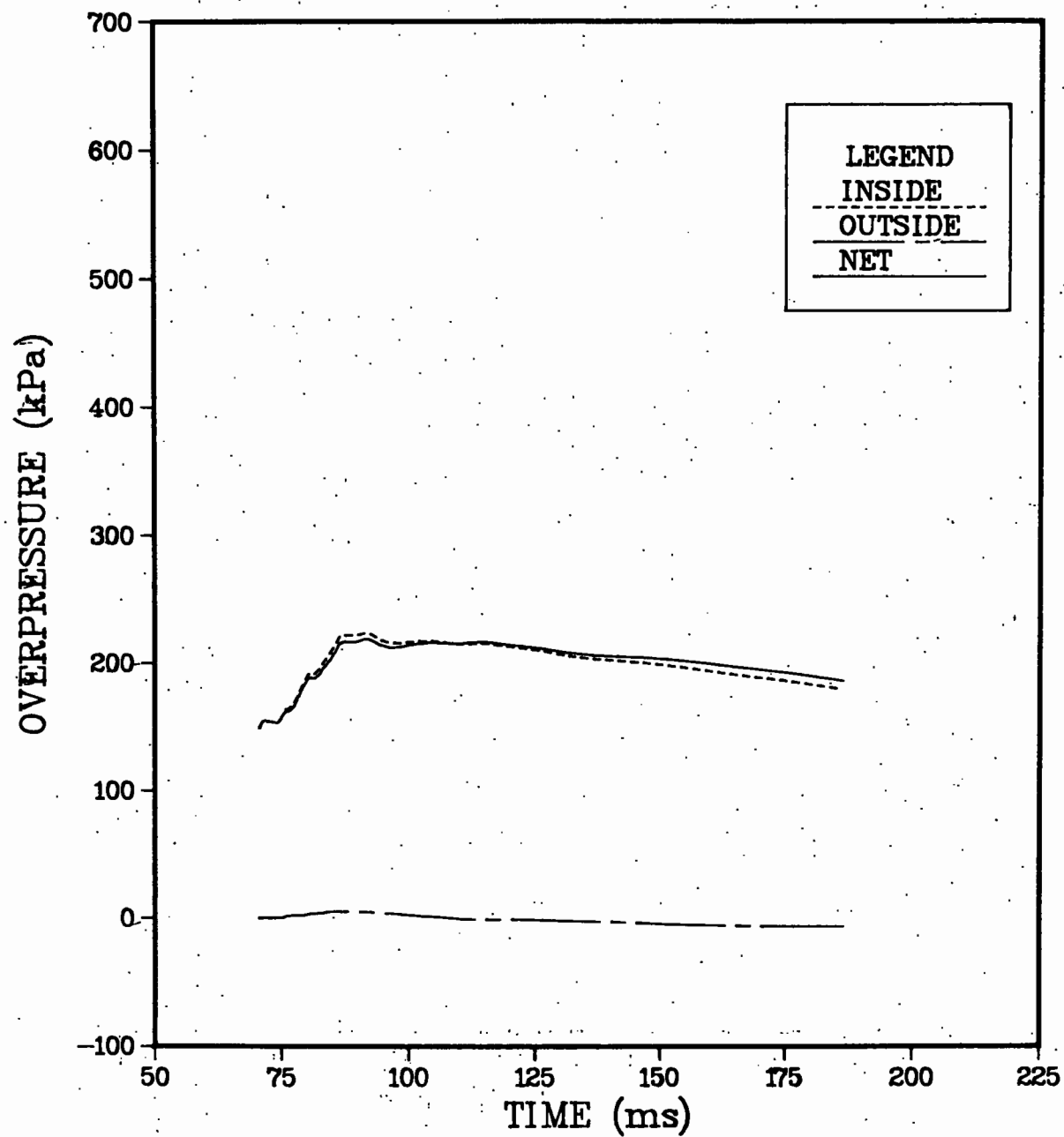


Figure 17b. Average Overpressure on the LB/TS Thick Side Wall Section, Excluding Open Side Vent Areas, Normal Vent.

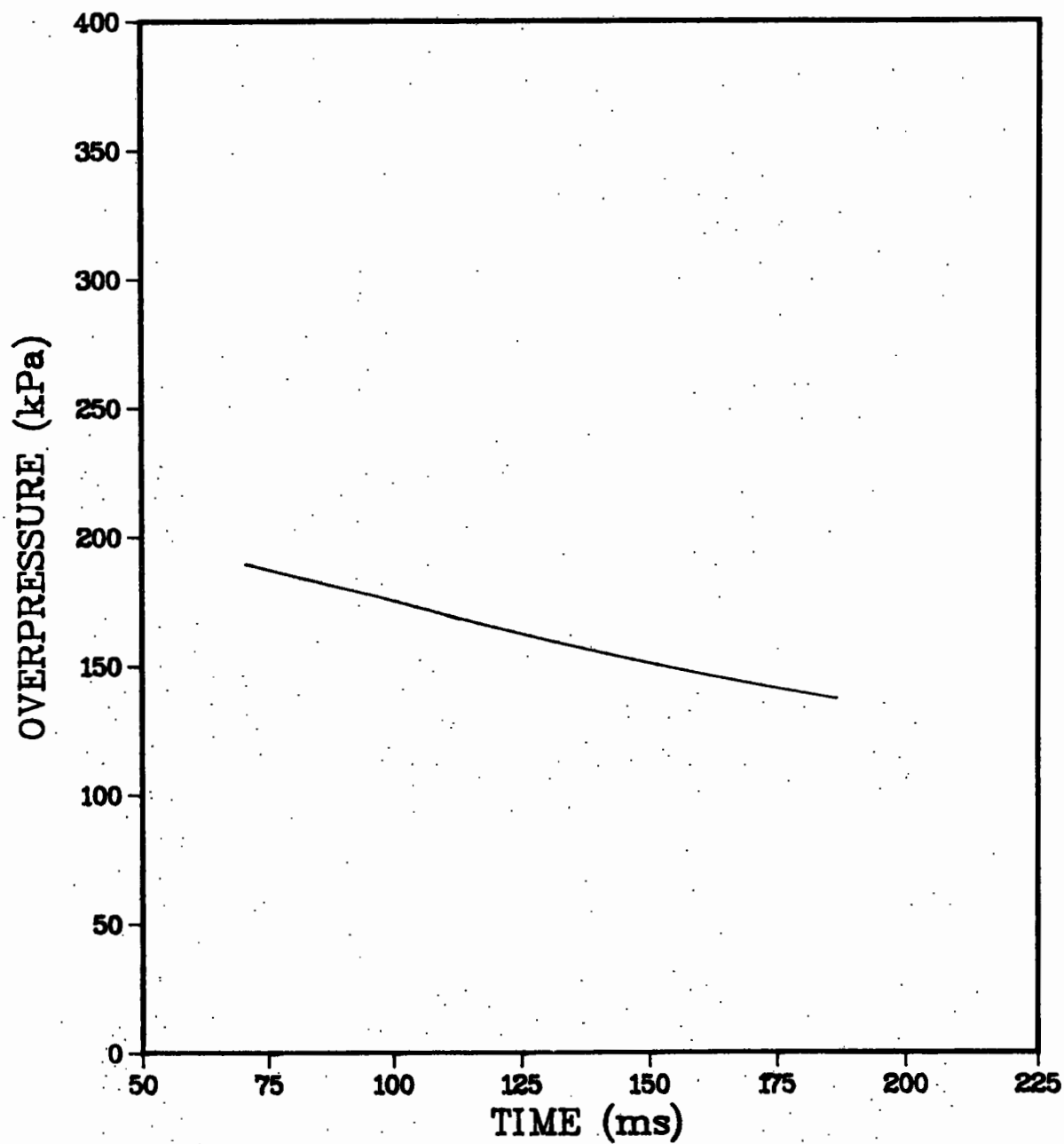


Figure 18a. Average Overpressure across the LB/TS Cross-Sectional Area at the Test Station, Low Vent.

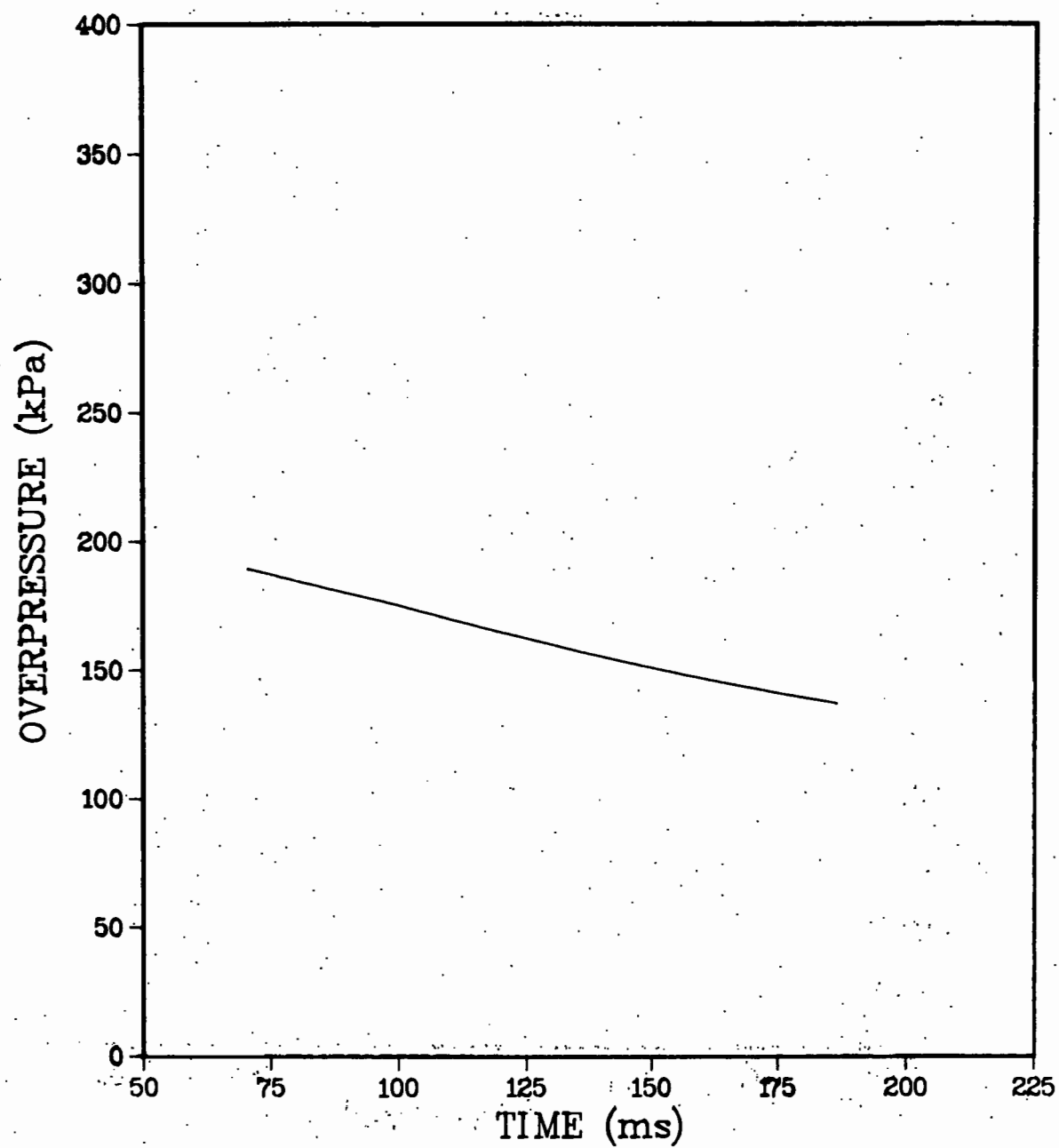


Figure 18b. Average Overpressure across the LB/TS Cross-Sectional Area at the Test Station, Normal Vent.

List of References

1. S. Gratiac and J. Monzac, "The Large Scale Nuclear Blast Simulator of the Gramat Research Center: (1) Concept, Research, Performance; (2) Description and Operational Utilization," Proceedings of the Seventh International Symposium on Military Applications of Blast Simulation, Medicine Hat, Alberta, Canada, 13-17 July 1981.
2. R.J. Pearson, K.O. Opalka, and D.M. Hisley, "Design Studies of Drivers for the US Large Blast/Thermal Simulator," Proceedings of the Ninth International Symposium on Military Applications of Blast Simulation, St. Edmund Hall, Oxford, England, 23-27 September 1985.
3. D.M. Hisley, E.J. Gion, and B.P. Bertrand, "Performance and Predictions for a Large Blast Simulator Model," US Army Ballistic Research Laboratory Technical Report BRL-TR-2647, Aberdeen Proving Ground, MD, April 1985. (AD#A158080)
4. K.O. Opalka and A. Mark, "The BRL-Q1D Code: A Tool for the Numerical Simulation of Flows in Shock Tubes with Variable Cross-Sectional Areas," US Army Ballistic Research Laboratory Technical Report BRL-TR-2763, Aberdeen Proving Ground, MD, October 1986. (AD#A174254)
5. K.O. Opalka, "Large Blast-Wave Simulators (LBS) with Cold-Gas Drivers: Computational Design Studies," US Army Ballistic Research Laboratory Technical Report BRL-TR-2786, Aberdeen Proving Ground, MD, March 1987. (AD#A181400)
6. D.M. Hisley, "Axisymmetric Calculations for the Large Blast/Thermal Simulator (LB/TS) Shock Tube Configuration," Proceedings of the Tenth International Symposium on Military Applications of Blast Simulation, Kurhaus-Bad Reichenhall, Federal Republic of Germany, 21-25 September 1987.
7. I. Osofsky, G. Mason, D. Hove, and D. McLaughlin, "Support of the Characterization of the LB/TS Facility," Defense Nuclear Agency Technical Report DNA-TR-85-259, Washington, D.C., August 1985. (AD#A182319)
8. D.M. Hisley, "A Computational Blast Valve Study," US Army Ballistic Research Laboratory Technical Report BRL-TR-2642, Aberdeen Proving Ground, MD, February 1985. (AD#A153050)
9. R.J. Pearson, "Large Blast Simulation," Society of Automotive Engineers Technical Paper, 1987 Aerotech Meeting, Long Beach, CA, 5-8 October 1987.
10. R. Guice and J. Gottlieb, "Passive and Active Reflection Eliminators," Proceedings of the Tenth International Symposium on Military Applications of Blast Simulation, Kurhaus-Bad Reichenhall, Federal Republic of Germany, 21-25 September 1987.
11. C.N. Kingery and G.A. Coulter, "Rarefaction Wave Eliminator Concepts for a Large Blast/Thermal Simulator," US Army Ballistic Research Laboratory Technical Report BRL-TR-2634, Aberdeen Proving Ground, MD, February 1985. (AD#A153073)
12. R.J. Pearson, private communication, US Army Ballistic Research Laboratory, Aberdeen Proving Ground, MD, May 1986.

List of References (Continued)

13. J.A. Hasdal, B.S. Chambers, and R.W. Clemens, "Support to BRL: HULL Code Implementation on a CDC 7600," SAI-80-701-AQ, Science Applications, Inc., McLean, VA, August 1979.
14. B.S. Chambers, III, and J.D. Wortman, "Two-Dimensional Shore (Partial Island) Cells for BRL HULL," US Army Ballistic Research Laboratory Contract Report ARBRL-CR-00497, Aberdeen Proving Ground, MD, December 1982. (AD#A1234357)
15. M.A. Fry, R.E. Durrett, G.P. Ganong, D.A. Matuska, M.D. Stucker, B.S. Chambers, C.E. Needham, and C.D. Westmoreland, "The HULL Hydrodynamics Computer Code," US Air Force Weapons Laboratory Technical Report AFWL-TR-76-183, September 1976. (AD#B014070L)
16. C.E. Needham and L.A. Wittwer, "The Air Force Weapons Laboratory Low Altitude Multiple Burst (LAMB) Model," US Air Force Weapons Laboratory, AFWL-DYT-75-2 (unpublished).
17. C.E. Needham, M.L. Havens, and C.S. Knauth, "Nuclear Blast Standard (1 KT)," US Air Force Weapons Laboratory Technical Report AFWL-TR-73-55 (Rev.), Kirtland Air Force Base, NM, April 1975. (AD#A014850)
18. J.D. Wortman and R.E. Lottero, "Comparison of HULL Hydrocode Computations of Shock Tube Blockage Effects on Target Loading for Step Shocks and Rapidly-Decaying Shocks," US Army Ballistic Research Laboratory Memorandum Report ARBRL-MR-03232, Aberdeen Proving Ground, MD, December 1982. (AD#123274)
19. N.H. Ethridge, R.E. Lottero, J.D. Wortman, B.P. Bertrand, "Flow Blockage and Its Effect on Minimum Incident Overpressure for Overturning Vehicles in a Large Blast Simulator," Proceedings of the Seventh International Symposium on Military Applications of Blast Simulation, Vol. II, Medicine Hat, Alberta, Canada, 13-17 July 1981.
20. N.H. Ethridge, R.E. Lottero, J.D. Wortman, and B.P. Bertrand, "HULL Hydrocode Computations of Flow Blockage and Its Relation to Overturning of Vehicles in a Large Blast Simulator," US Army Ballistic Research Laboratory Technical Report ARBRL-TR-02442, Aberdeen Proving Ground, MD, November 1982. (AD#069766L)
21. N.H. Ethridge, R.E. Lottero, J.D. Wortman, and B.P. Bertrand, "Blockage Effects in a Large Blast Simulator," Proceedings of the Eighth International Symposium on Military Applications of Blast Simulation, Spiez, Switzerland, 20-24 June 1983.
22. N.H. Ethridge, R.E. Lottero, J.D. Wortman, and B.P. Bertrand, "Computational and Experimental Studies of Blockage Effects in a Blast Simulator," US Army Ballistic Research Laboratory Technical Report ARBRL-TR-02564, Aberdeen Proving Ground, MD, June 1984. (AD#A143457)
23. L. Lamport, "L^AT_EX, A Document Publishing System," Addison-Wesley Publishing Company, Inc., Fifth Printing, September 1986, Copyright 1986.

DISTRIBUTION LIST

<u>No. of</u> <u>Copies</u>	<u>Organization</u>	<u>No. of</u> <u>Copies</u>	<u>Organization</u>
12	Administrator Defense Technical Information Center ATTN: DTIC-FDAC Cameron Station, Bldg 5 Alexandria, VA 22304-6145	9	Director Defense Nuclear Agency ATTN: DDST TIPL/Tech Lib SPSS/K. Goering SPTD/T. Kennedy SPAS/P.R. Rohr G. Ullrich STSP/COL Kovel NATD NATA Washington, DC 20305
1	Director of Defense Research & Engineering ATTN: DD/TWP Washington, DC 20301	2	Commander Field Command Defense Nuclear Agency ATTN: FCPR FCTMOF Kirtland AFB, NM 87115
1	Asst. to the Secretary of Defense (Atomic Energy) ATTN: Document Control Washington, DC 20301	1	Commander Field Command, DNA Livermore Branch ATTN: FCPRL P.O. Box 808 Livermore, CA 94550
1	Director Defense Advanced Research Projects Agency ATTN: Tech Lib 1400 Wilson Boulevard Arlington, VA 22209	1	HQDA (DAMA-ART-M) Washington, DC 20310
2	Director Federal Emergency Management Agency ATTN: D. A. Bettge Technical Library Washington, DC 20472	10	C.I.A. OIR/DB/Standard GE47 HQ Washington, D.C. 20505
1	Director Defense Intelligence Agency ATTN: DT-2/Wpns & Sys Div Washington, DC 20301	1	Program Manager US Army BMD Program Office ATTN: John Shea 5001 Eisenhower Avenue Alexandria, VA 22333
1	Director National Security Agency ATTN: E. F. Butala, R15 Ft. George G. Meade, MD 20755	2	Commander US Army BMD Advanced Technology Center ATTN: CRDABH-X CRDABH-S P.O. Box 1500 Huntsville, AL 35807
1	Director Joint Strategic Target Planning Staff JCS Offut AFB Omaha, NB 68113		

DISTRIBUTION LIST

<u>No. of Copies</u>	<u>Organization</u>	<u>No. of Copies</u>	<u>Organization</u>
1	Commander US Army BMD Command ATTN: BDMSC-TFN/N.J. Hurst P.O. Box 1500 Huntsville, AL 35807	1	U.S. Army Armament, Munitions and Chemical Command ATTN: AMSMC-IMP-L Rock Island, IL 61299-7300
1	Commander US Army Engineer Division ATTN: HNDED-FD P.O. Box 1500 Huntsville, AL 35807	1	Commander US AMCCOM ARDEC CCAC Benet Weapons Laboratory ATTN: SMCAR-CCB-TL Watervliet, NY 12189-4050
2	Deputy Chief of Staff for Operations and Plans ATTN: Technical Library Director of Chemical & Nuc Operations Department of the Army Washington, DC 20310	1	Commander U.S. Army Aviation Systems Command ATTN: AMSAV-ES 4300 Goodfellow Blvd. St. Louis, MO 63120-1798
3	Director US Army Engineer Waterways Experiment Station ATTN: Technical Library Jim Watt Jim Ingram P.O. Box 631 Vicksburg, MS 39180-0631	1	Director U.S. Army Aviation Research and Technology Activity Ames Research Center Moffett Field, CA 94035-1099
1	Commander US Army Materiel Command ATTN: AMCDRA-ST 5001 Eisenhower Avenue Alexandria, VA 22333-0001	1	Commander US Army Communications - Electronics Command ATTN: AMSEL-ED Fort Monmouth, NJ 07703-5301
1	Commander US Army Armament Research, Development and Engineering Center ATTN: SMCAR-MSI Dover, NJ 07801-5001	1	Commander US Army Communications Rsch and Development Command ATTN: DRSEL-ATDD Fort Monmouth, NJ 07703
1	Commander US Army Armament Research, Development and Engineering Center ATTN: SMCAR-TDC Dover, NJ 07801	1	Commander CECOM R&D Technical Library ATTN: AMSEL-IM-L (Reports Section) B.2700 Fort Monmouth, NJ 07703-5301
		2	Commander US Army Electronics Research and Development Command ATTN: DELEW-E, W. S. McAfee DELSA-EI, J. Roma Fort Monmouth, NJ 07703-5301

DISTRIBUTION LIST

<u>No. of</u> <u>Copies</u>	<u>Organization</u>	<u>No. of</u> <u>Copies</u>	<u>Organization</u>
6	Director US Army Harry Diamond Labs ATTN: Mr. James Gaul Mr. L. Belliveau Mr. J. Meszaros Mr. J. Gwaltney Mr. Bill Vault Mr. R. J. Bostak 2800 Powder Mill Road Adelphi, MD 20783-1197	1	Commander US Army Logistics Management Center ATTN: ATCL-O, Mr. Robert Cameron Fort Lee, VA 23801
4	Director US Army Harry Diamond Labs ATTN: SLCHD-TA-L DRXDO-TI/002 DRXDO-NP SLCHD-RBA/J. Rosado 2800 Powder Mill Road Adelphi, MD 20783-1197	2	Commander US Army Materials Technology Laboratory ATTN: AMXMR-ATL Eugene de Luca Watertown, MA 02172-0001
1	Commander US Army Missile Command ATTN: AMSMI-RD Redstone Arsenal, AL 35898-5245	1	Commander US Army Research Office ATTN: SLCRO-D P.O. Box 12211 Research Triangle Park NC 27709-2211
1	Director US Army Missile and Space Intelligence Center ATTN: AIAMS-YDL Redstone Arsenal, AL 35898-5500	4	Commander US Army Nuclear & Chemical Agency ATTN: ACTA-NAW MONA-WE Technical Library LTC Finno 7500 Backlick Rd, Bldg. 2073 Springfield, VA 22150
2	Commander US Army Natick Research and Development Center ATTN: AMDNA-D/Dr. D. Sieling STRNC-UE/J. Calligeros Natick, MA 01762	1	Commander US Army TRADOC ATTN: DCST&E Fort Monroe, VA 23651
1	Commander US Army Tank-Automotive Command ATTN: AMSTA-TSL Warren, MI 48397-5000	2	Director US Army TRADOC Systems Analysis Activity ATTN: LTC John Hesse ATOR-TSL White Sands Missile Range, NM 88002-5502
1	Commander US Army Foreign Science and Technology Center ATTN: Research and Data Br 220 7th Street, NE Charlottesville, VA 22901	2	Commandant U.S. Army Infantry School ATTN: ATSH-CD-CS-OR Fort Benning, GA 31905-5400

DISTRIBUTION LIST

<u>No. of Copies</u>	<u>Organization</u>	<u>No. of Copies</u>	<u>Organization</u>
1	Commander U.S. Army Development and Employment Agency ATTN: MODE-ORO Fort Lewis, WA 98433-5000	1	Commander Naval Sea Systems Command ATTN: Code SEA-62R Department of the Navy Washington, DC 20362-5101
1	Commandant Interservice Nuclear Weapons School ATTN: Technical Library Kirtland AFB, NM 87115	3	Officer-in-Charge (Code L31) Civil Engineering Laboratory Naval Construction Battalion Center ATTN: Stan Takahashi R. J. Odello Technical Library Port Hueneme, CA 93041
1	Chief of Naval Material ATTN: MAT 0323 Department of the Navy Arlington, VA 22217	1	Commander David W. Taylor Naval Ship Research & Development Command ATTN: Lib Div, Code 522 Bethesda, MD 20084-5000
2	Chief of Naval Operations ATTN: OP-03EG OP-985F Department of the Navy Washington, DC 20350	1	Commander Naval Surface Weapons Center ATTN: DX-21, Library Br. Dahlgren, VA 22448-5000
1	Chief of Naval Research ATTN: N. Perrone Department of the Navy Arlington, VA 22217	2	Commander Naval Surface Weapons Center ATTN: Code WA501/Navy Nuclear Programs Office Code WX21/Tech Library Silver Spring, MD 20902-5000
1	Director Strategic Systems Projects Ofc ATTN: NSP-43, Tech Library Department of the Navy Washington, DC 20360	1	Commander Naval Weapons Center ATTN: Code 533, Tech Lib China Lake, CA 93555-6001
1	Commander Naval Electronic Systems Com ATTN: PME 117-21A Washington, DC 20360	1	Commander Naval Weapons Evaluation Fac ATTN: Document Control Kirtland AFB, NM 87117
1	Commander Naval Facilities Engineering Command Washington, DC 20360	1	Commander Naval Research Laboratory ATTN: Code 2027, Tech Lib Washington, DC 20375

DISTRIBUTION LIST

<u>No. of Copies</u>	<u>Organization</u>	<u>No. of Copies</u>	<u>Organization</u>
1	Superintendent Naval Postgraduate School ATTN: Code 2124, Technical Reports Library Monterey, CA 93940	1	Director Lawrence Livermore Lab. ATTN: Tech Info Dept L-3 P.O. Box 808 Livermore, CA 94550
1	AFSC/SDOA Andrews Air Force Base MD 20334	2	Director Los Alamos Scientific Lab. ATTN: Doc Control for Rpts Lib P.O. Box 1663 Los Alamos, NM 87545
1	AFWL/SUL Kirtland AFB, NM 87117	2	Director Sandia National Laboratories ATTN: Doc Control for 3141 Sandia Rpt Collection L. J. Vortman P.O. Box 5800 Albuquerque, NM 87185-5800
1	AFATL/DOIL (Tech Info Center) Eglin AFB, FL 32542-5438	1	Director Sandia Laboratories Livermore Laboratory ATTN: Doc Control for Technical Library P.O. Box 969 Livermore, CA 94550
1	AFESC/RDCS ATTN: Paul Rosengren Tyndall AFB, FL 32403	1	Director National Aeronautics and Space Administration Scientific & Tech Info Fac P.O. Box 8757 Baltimore/Washington International Airport MD 21240
1	AFATL (DLYV) Eglin AFB, FL 32542-5438	1	Director NASA-Ames Research Center Applied Computational Aerodynamics Branch MS 202-14, Dr. T. Holtz Moffett Field, CA 94035
1	RADC (EMTLD/Docu Library) Griffiss AFB, NY 13441		
1	AFWL/NTES, R. Henny Kirtland AFB, NM 87117-6008		
1	AFWL/NTED, J. W. Aubrey Kirtland AFB, NM 87117-6008		
2	Commander-in-Chief Strategic Air Command ATTN: NRI-STINFO Lib Offutt AFB, NB 68113		
1	AFIT (Lib Bldg. 640, Area B) Wright-Patterson AFB Ohio 45433		
1	FTD/NIIS Wright-Patterson AFB Ohio 45433		

DISTRIBUTION LIST

<u>No. of Copies</u>	<u>Organization</u>	<u>No. of Copies</u>	<u>Organization</u>
3	Aberdeen Research Center ATTN: N.H. Ethridge J. Keefer Library P.O. Box 548 30 Diamond Street Aberdeen, MD 21001	1	Goodyear Aerospace Corp ATTN: R. M. Brown, Bldg 1 Shelter Engineering Litchfield Park, AZ 85340
1	Aerospace Corporation ATTN: Tech Info Services P.O. Box 92957 Los Angeles, CA 90009	6	Kaman Avidyne ATTN: Dr. R. Reutenick (4 cys) Mr. S. Criscione Mr. R. Milligan 83 Second Avenue Northwest Industrial Park Burlington, MA 01830
1	Agbabian Associates ATTN: M. Agbabian 250 North Nash Street El Segundo, CA 90245	3	Kaman Sciences Corporation ATTN: Library P. A. Ellis F. H. Shelton 1500 Garden of the Gods Road Colorado Springs, CO 80907
1	The BDM Corporation ATTN: Richard Hensley P.O. Box 9274 Albuquerque International Albuquerque, NM 87119	2	Kaman-TEMPO ATTN: DASIAC Don Sachs P.O. Drawer QQ 816 State Street Santa Barbara, CA 93102
1	The Boeing Company ATTN: Aerospace Library P.O. Box 3707 Seattle, WA 98124	1	Lockheed Missiles & Space Co. ATTN: J. J. Murphy, Dept. 81-11, Bldg. 154 P.O. Box 504 Sunnyvale, CA 94086
1	California Research and Technology ATTN: F. Sauer Suite B 130 11875 Dublin Blvd Dublin, CA 94568	1	Martin Marietta Aerospace Orlando Division ATTN: G. Fotieo P.O. Box 5837 Orlando, FL 32805
1	California Research & Technology, Inc. ATTN: M. Rosenblatt 20943 Devonshire Street Chatsworth, CA 91311	2	McDonnell Douglas Astronautics Corporation ATTN: Robert W. Halprin K.A. Heinly 5301 Bolsa Avenue Huntington Beach, CA 92647
1	Carpenter Research Corporation ATTN: H. Jerry Carpenter Suite 424 904 Silver Spur Road Rolling Hills Estates, CA 90274		

DISTRIBUTION LIST

<u>No. of Copies</u>	<u>Organization</u>	<u>No. of Copies</u>	<u>Organization</u>
1	New Mexico Engineering Research Institute (CERF) ATTN: J. Leigh P.O. Box 25 UNM Albuquerque, NM 87131	1	Texas Engineering Experiment Station ATTN: Dr. D. Anderson 301 Engineering Research Center College Station, TX 77843
2	Physics International Corp 2700 Merced Street San Leandro, CA 94577	2	TRW Systems Group ATTN: Benjamin Sussholtz Stanton Fink One Space Park Redondo Beach, CA 90278
2	R&D Associates ATTN: Technical Library Allan Kuhl P.O. Box 9695 Marina del Rey, CA 90291	1	Battelle Memorial Institute ATTN: Technical Library 505 King Avenue Columbus, OH 43201
1	R&D Associates ATTN: G.P. Ganong P.O. Box 9335 Albuquerque, NM 87119	1	California Inst of Tech ATTN: T. J. Ahrens 1201 E. California Blvd. Pasadena, CA 91109
2	Science Applications, Inc. ATTN: W. Layson John Cockayne PO BOX 1303 1710 Goodridge Drive McLean, VA 22102	2	Denver Research Institute University of Denver ATTN: Mr. J. Wisotski Technical Library PO Box 10127 Denver, CO 80210
1	Science Applications, Inc. ATTN: Technical Library 1250 Prospect Plaza La Jolla, CA 92037	1	TRW Ballistic Missile Division ATTN: H. Korman, Mail Station 526/614 P.O. Box 1310 San Bernadino, CA 92402
2	Systems, Science and Software ATTN: C. E. Needham Lynn Kennedy PO Box 8243 Albuquerque, NM 87198	1	Massachusetts Institute of Technology Aeroelastic and Structures Research Laboratory ATTN: Dr. E. A. Witmer Cambridge, MA 02139
3	Systems, Science and Software ATTN: Technical Library R. Duff K. Pyatt PO Box 1620 La Jolla, CA 92037	2	Southwest Research Institute ATTN: Dr. W. E. Baker A. B. Wenzel 8500 Culebra Road San Antonio, TX 78228

DISTRIBUTION LIST

<u>No. of Copies</u>	<u>Organization</u>
--------------------------	---------------------

- | | |
|---|---|
| 1 | SRI International
ATTN: Dr. G. R.
Abrahamson
333 Ravenswood Avenue
Menlo Park, CA 94025 |
| 1 | Stanford University
ATTN: Dr. D. Bershader
Durand Laboratory
Stanford, CA 94305 |

Aberdeen Proving Ground

Dir, USAMSAA
ATTN: AMXSY-D
AMXSY-MP, H. Cohen
Cdr, USATECOM
ATTN: AMSTE-SI-F
Cdr, CRDC, AMCCOM
ATTN: SMCCR-RSP-A
SMCCR-MU
SMCCR-SPS-IL

USER EVALUATION SHEET/CHANGE OF ADDRESS

This Laboratory undertakes a continuing effort to improve the quality of the reports it publishes. Your comments/answers to the items/questions below will aid us in our efforts.

1. BRL Report Number _____ Date of Report _____
2. Date Report Received _____
3. Does this report satisfy a need? (Comment on purpose, related project, or other area of interest for which the report will be used.) _____

4. How specifically, is the report being used? (Information source, design data, procedure, source of ideas, etc.) _____

5. Has the information in this report led to any quantitative savings as far as man-hours or dollars saved, operating costs avoided or efficiencies achieved, etc? If so, please elaborate. _____

6. General Comments. What do you think should be changed to improve future reports? (Indicate changes to organization, technical content, format, etc.) _____

CURRENT
ADDRESS

Name

Organization

Address

City, State, Zip

7. If indicating a Change of Address or Address Correction, please provide the New or Correct Address in Block 6 above and the Old or Incorrect address below.

OLD
ADDRESS

Name

Organization

Address

City, State, Zip

(Remove this sheet, fold as indicated, staple or tape closed, and mail.)

----- FOLD HERE -----

Director
U.S. Army Ballistic Research Laboratory
ATTN: SLCBR-DD-T
Aberdeen Proving Ground, MD 21005-5066



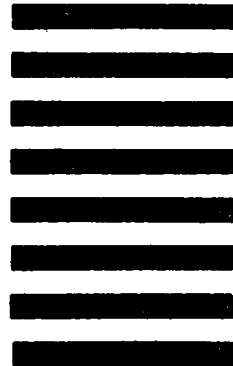
NO POSTAGE
NECESSARY
IF MAILED
IN THE
UNITED STATES

OFFICIAL BUSINESS

PENALTY FOR PRIVATE USE, \$300

BUSINESS REPLY MAIL
FIRST CLASS PERMIT NO 12062 WASHINGTON, DC
POSTAGE WILL BE PAID BY DEPARTMENT OF THE ARMY

Director
U.S. Army Ballistic Research Laboratory
ATTN: SLCBR-DD-T
Aberdeen Proving Ground, MD 21005-9989



----- FOLD HERE -----



U.S. OFFICIAL MAIL
U.S. POSTAGE
0.90

DA Label 18-1, Sep 83
Edition of Oct 74 will be used until exhausted.

DEPARTMENT OF THE ARMY
Director, USA Ballistic Research Lab
ATTN: SLCBR-DD-T
Aberdeen Proving Ground, MD 21005-5066
OFFICIAL BUSINESS
PENALTY FOR PRIVATE USE. \$300

SPECIAL

Battelle Memorial Institute
ATTN: Technical Library
505 King Avenue
Columbus, OH 43201